AGU PUBLICATIONS

JGR

Journal of Geophysical Research: Solid Earth

RESEARCH ARTICLE
10.1002/2016JB012905

**Key Points:**
- Analytical expressions for magma reservoir overpressure and surface displacements are derived using a brittle elastic damage model
- Seismicity and displacements in the volcanic edifice are well fitted by this damage model
- Pre-eruptive shear modulus decrease controls magma overpressure. Power strain maxima allow defining times supporting eruption prediction

**Supporting Information:**
- Supporting Information S1
- Supporting Information S2

**Correspondence to:**
J.-L. Got,
jlgot@univ-savoie.fr

**Citation:**
Got, J.-L., A. Carrier, D. Marsan, F. Jouanne, K. Vogfjörd, and T. Villemin (2017), An analysis of the nonlinear magma-edifice coupling at Grimsvötn volcano (Iceland), *J. Geophys. Res. Solid Earth*, *122*, doi:10.1002/2016JB012905.

Received 9 FEB 2016
Accepted 3 JAN 2017
Accepted article online 6 JAN 2017



# An analysis of the nonlinear magma-edifice coupling at Grimsvötn volcano (Iceland)

**Jean-Luc Got[1,2], Aurore Carrier[1,2], David Marsan[1,2], François Jouanne[1,2], Kristin Vogfjörd[3], and Thierry Villemin[4]**

[1]Université Savoie Mont-Blanc, ISTerre, Le Bourget-du-Lac, France, [2]CNRS, ISTerre, Le Bourget-du-Lac, France, [3]Icelandic Meteorological Office, Reykjavik, Iceland, [4]Université Savoie Mont-Blanc, EDYTEM, Le Bourget-du-Lac, France

**Abstract** Continuous monitoring of seismicity and surface displacement of active volcanoes can reveal important features of the eruptive cycle. Here high-quality GPS and earthquake data recorded at Grimsvötn volcano by the Icelandic Meteorological Office during the 2004–2011 intereruptive period are analyzed. These showed a characteristic pattern, with an initial ~2 year long exponential decay followed by ~3 year long constant surface displacement inflation rate. We model it by using a one magma reservoir model in an elastic damaging edifice, with incompressible magma and constant pressure at the base of the magma conduit. Seismicity rate and damage were first modeled, and simple analytical expressions were derived for the magma reservoir overpressure and surface displacement as functions of time. Very good fits of the seismicity and surface displacement data were obtained by fitting only three phenomenological parameters. Characteristic time and power strain show maxima from which reference times were inferred that split the intereruptive period into five periods. After the pressurization periods, damage occurring in the third period induced weakly nonlinear variations in magma overpressure and flow, and surface displacement. During the fourth period, the damage dominated and variations became more strongly nonlinear, the reservoir overpressure decreased, and magma flow increased. This process lasted until the power strain reached its second maximum, where instability was generalized. This maximum is a physical limit, the occurrence of which shortly precedes rupture and, eventually, eruption. This analysis allows characterization of the state of the volcanic edifice during the intereruptive period and supports medium-term prediction of rupture and eruption.

## 1. Introduction

Improvements to surface displacement measurements have provided long time series that sample the surface deformation of some volcanoes sufficiently well to allow a part of their internal dynamics to be inferred, especially through satellite measurements such as continuous GPS and interferometric synthetic aperture radar. This is the case for some well-instrumented basaltic shield volcanoes in Hawaii, Iceland, and La Réunion Island and for Etna volcano, where a shallow-level magma reservoir lies in or immediately below their edifices. Most of these volcanoes show pre-eruptive inflation and co-eruptive deflation [see, e.g., *Schmid et al.*, 2012]. Pre-eruptive inflation carries information on the feeding system and the magma-edifice interaction. Various patterns can be observed, which often correspond to only part of the complete intereruptive process. Therefore, the study of well-recorded, complete intereruptive sequences can be particularly instructive. Surface displacement time series that show large parts of intereruptive processes have already been studied and reported, by, e.g., *Lu et al.* [2003] at Westdahl volcano (Alaska) and *Sturkell et al.* [2006] at Krafla volcano (Iceland). Both of these studies showed that the rate of inflation was best represented by an exponential decay, which corresponded to the magma replenishment and pressurization of a shallow-level reservoir. Sometimes this exponential decay was followed by a constant inflation rate [see, e.g., *Sturkell et al.*, 2006]. However, the best records we know of a complete intereruptive process that shows this pattern of exponential decay followed by a constant inflation rate over a timescale of years are those for Grimsvötn volcano (Iceland). This simple and remarkable pattern has made these data an archetype for the displacement that can be recorded at the surface of an initially stable basaltic volcano that is pressurized by a shallow-level magma reservoir. This was recently studied by *Reverso et al.* [2014] and interpreted as the evidence of a two-magma-chamber pressurized structure in a linear elastic medium, under the condition of a constant magma flow from depth.

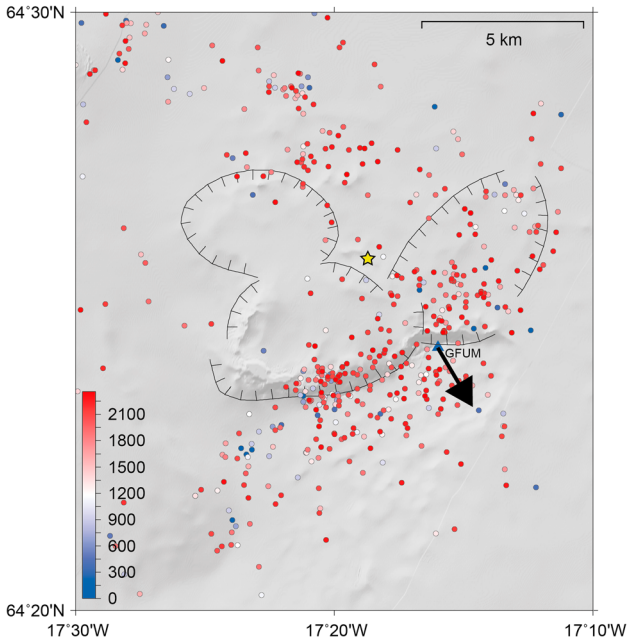


**Figure 1.** Map of the caldera complex of the Grimsvötn volcano, showing the location of the GFUM permanent GPS station (black triangle) on Grimsfjall and the rims of the Grimsvötn caldera (from *Gudmundsson and Milsom* [1997]). The vector shows the direction of the horizontal displacement recorded at GFUM from 1 December 2004 to 21 May 2011. Dots represent the earthquakes recorded by the IMO (Icelandic Meteorological Office) seismic network at Grimsvötn caldera during the same time period, and dot color represents the time in days from 1 December 2004. Yellow star is the center of the magma reservoir estimated from *Hreinsdottir et al.* [2014].

This constant magma flow in such a linear elastic structure implies infinitely growing pressure in the magma chambers.

However, rock strength is limited, and inelastic deformation occurs progressively, which eventually leads to rupture followed by eruption or intrusion. Rock mechanics experiments have shown that macrorupture at the sample scale does not occur without prior perturbation of the medium; deformation and microruptures occur instead before the stress in the sample reaches its peak strength [see, e.g., *Jaeger et al.*, 2007]. An accelerating number of microruptures characterizes the state of a sample close to failure during the tertiary creep stage [*Cox and Meredith*, 1993; *Main*, 2000; *Amitrano and Helmstetter*, 2006]. This progressive rupture process lowers the sample strength and its elastic properties, which is known as brittle damage. This process has been studied intensely in material sciences [see, e.g., *Kachanov*, 1958; *Lemaitre*, 1994], and more recently in earth sciences [e.g., *Lyakhovsky et al.*, 1997; *Turcotte and Glasscoe*, 2004; *Amitrano and Helmstetter*, 2006; *Heap et al.*, 2010].

At the scale of the volcanic edifice, the rupture that also takes place before an eruption is in the form of earthquakes, and a similar damage process is expected. Eruption prediction methods that are directly derived from the study of tertiary creep under constant load, such as the failure forecast method [*Voight*, 1988; *Tarraga et al.*, 2008; *Bell et al.*, 2011]), have used pre-eruptive seismicity to forecast eruptions [see also *Kilburn*, 2003]. The progressive and damaging character of the rupture process should therefore be taken into account in the modeling of pre-eruptive processes, as the damage can decrease the elastic characteristics of the edifice. Magma-edifice coupling and edifice damage should be taken into account in the model, and seismicity and surface displacement should be used jointly to constrain such models. This approach was followed by *Carrier et al.* [2015] in the numerical modeling of surface displacements measured near the summit of Piton de la Fournaise volcano (La Réunion Island) before its major eruption of February–March 2007. In the present study, we have gone a step further in the modeling and the understanding of the dynamics of the pre-eruptive deformation process, and an analytical solution is found using simple pressurization and damage models.

Grimsvötn volcano (Iceland) is an active basaltic volcano that is part of a large volcanic complex, the activity of which is induced by the Icelandic hot spot and the mid-Atlantic rift. It is located 20–30 km west of the center of Vatnajökull glacier, and it reaches an altitude of 1725 m, where it forms a 6 km to 12 km large, 250 m deep, clover-shaped caldera complex [*Björnsson and Einarsson*, 1990; *Gudmundsson and Milsom*, 1997],

which is mostly filled by the glacier and partially by a lake (Figure 1). Most of this edifice is subglacial, and the maximal thickness of the Vatnajökull glacier is 1000 m.

A shallow magma reservoir has been evidenced below the caldera using GPS measurements [*Sturkell et al.*, 2003, 2006; *Hreinsdottir et al.*, 2014] and tomographic inversion [*Alfaro et al.*, 2007], and it was estimated to be located at a depth of 3 km to 4 km [*Alfaro et al.*, 2007] or possibly shallower at a depth of 1.7 km [*Hreinsdottir et al.*, 2014]. *Alfaro et al.* [2007] inferred that the reservoir might have a sill geometry at 7 km to 8 km (E-W) long, 4 km to 5 km (N-S) wide, and 1 km thick. NE-SW fissure swarms diverge from the SW caldera and continue in the direction of the 25 km long Lakagigar eruptive fissure, which is considered to be a part of the Grimsvötn volcanic system. Regional extensional stress is assumed to be roughly perpendicular to the rift.

Grimsvötn volcano is the most frequently erupting volcano in Iceland, with the most recent confirmed eruptions during 1934, 1983, 1998, 2004, and 2011. The 21–28 May 2011 eruption was the most energetic in the last 100 years. This occurred along an EW oriented eruptive fissure that is in the southern part of the caldera, close to the fissure that was activated during the 2004 eruption [see, e.g., *Vogfjörd et al.*, 2005]. Earthquake swarms prior to the 2004 and 2011 eruptions allowed short-term prediction and warning of these eruptions. A jökulhlaup that preceded the 2004 eruption also allowed medium-term alert [e.g., *Vogfjörd et al.*, 2005]. The effects of the unloading of the shallow-level magma reservoir by jökulhlaups immediately before an eruption were studied by *Albino et al.* [2010] using linear elastic models.

## 2. Data

### 2.1. Deformation Data

At Grimsvötn volcano (Iceland), the surface displacement is recorded since 2004 at the GFUM permanent GPS station, which is located near the rim of the main caldera, at about 3–4 km from the center of the caldera and reservoir axis (Figure 1). This time series was processed and used by *Reverso et al.* [2014]. Daily site positions were obtained using the International Global Navigation Satellite System Service precise orbits [*Beutler et al.*, 1999], international GPS services Earth rotation parameters, and data from nearby permanent GPS stations. Absolute antenna phase center offset models were used during this analysis [*Bilich et al.*, 2012]. The reference frame is the plate boundary between Eurasia and North America, which was determined using the rotation poles relative to International Terrestrial Reference Frame 2008. This time series once in plate boundary reference frame has been corrected for tectonic motion using a simulation of interrifting deformation constrained by GPS velocities (without GFUM velocity), considering that the plate boundary can be simulated by a dyke locked at depth (see *Reverso et al.* [2014] for an extensive presentation of the processing of these data). The vertical displacements at GFUM contain a seasonal component, which is a pattern that was already observed at Katla volcano for at least 40 years; see, e.g., *Tryggvason* [1973]. These were not used in the present study as with *Reverso et al.* [2014]. The horizontal surface displacements computed at GFUM from 1 December 2004, were less affected by seasonal variations. The horizontal displacement norm (Figure 2) showed a clear intereruptive inflation that was composed of a $\sim$ 2 year long exponential decay rate that was followed by a steady displacement rate over the next $\sim$ 5 years, with a constant N140 direction.

### 2.2. Seismicity Data

The earthquakes located by the Icelandic Meteorological Office seismic network during the same time period (2004–2011) were analyzed (from 55 three-component stations that were recording at 100 Hz sampling frequency [*Vogfjörd et al.*, 2005]). The present study considered the 651 earthquakes located around the Grimsvötn caldera (Figure 1). The local magnitude completeness of the catalog is $M_c = 1.3$, and the maximum likelihood estimation of the $b$ value is 0.95, which is close to the value of 1 that is commonly found in seismically active regions [see, e.g., *Roberts et al.*, 2015]. The magnitudes were used to compute the rupture length for each earthquake, with the assumption of the scaling relationships established by *Wells and Coppersmith* [1994]. The computation of the area ruptured by each of the 533 $M_l \geq 1.3$ earthquakes that occurred between 1 December 2004 and 21 May 2011 showed that their rupture area and rupture length were roughly constant (Figure S1 in the supporting information). This small and constant rupture area or length, and its direct computation by taking into account its probability distribution function, shows that the more frequent, small-magnitude, earthquakes dominated the rupture process.

The cumulative number of earthquakes as a function of time shows a clear acceleration (Figure 2). This pattern appears not to be related to the long, steady displacement rate recorded at the surface. In the following paragraphs, we show how both patterns (accelerating earthquake number and constant rate surface displacement

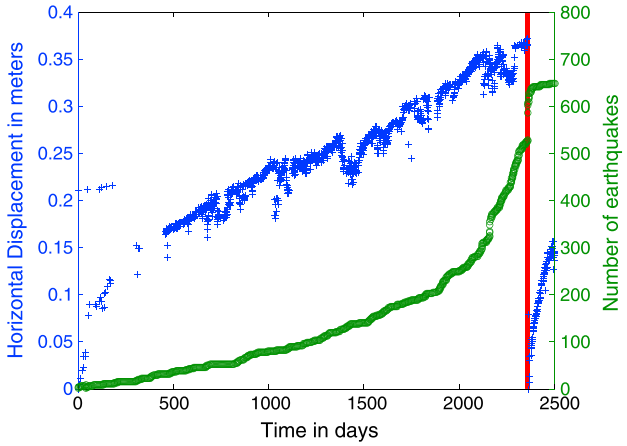


**Figure 2.** Horizontal displacement norm in meters recorded at the GFUM GPS station (blue crosses) and cumulative seismicity recorded by the IMO network (green circles), as functions of time in days from 1 December 2004 (end of the 2004 coeruptive deflation) to 31 December 2011 at Grimsvötn volcano. The 2011 eruption of Grimsvötn volcano occurred on May 21 (vertical red line).

over 5 years) can nevertheless be in agreement and can be understood within a unique and simple model that involves volcanic edifice pressurization and damage.

## 3. Model

### 3.1. Modeling Pressurization of a Damageable Volcanic Edifice

In the present model, a unique, shallow-level, pressurized spherical magma reservoir is fed by a cylindrical vertical magma conduit in a damageable elastic half-space (Figure 3). The magma pressure is constant at the base of the conduit. This is a two-dimensional axisymmetric homogeneous and isotropic model that is similar to the one used in *Lengliné et al.* [2008] and *Carrier et al.* [2015].

Therefore, a closed magma-feeding system was considered in which the medium can be damaged by the pressurization of the reservoir, so that the shear modulus $G$ of the edifice can vary with time. Damage is homogeneous and isotropic in the elastic half-space. The magma is considered to be incompressible, and there is

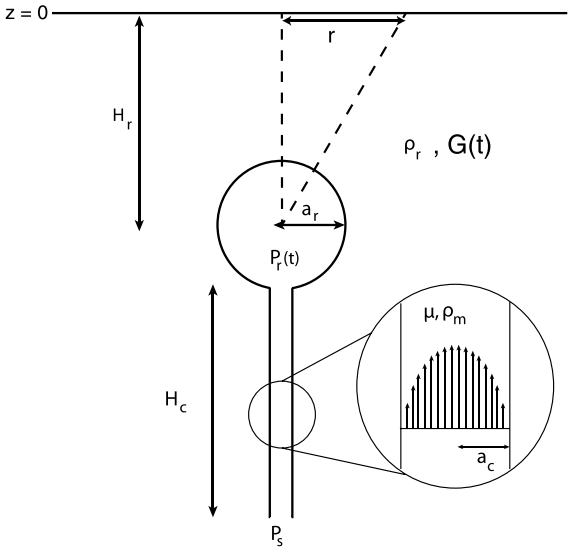


**Figure 3.** Physical model used in this study [from *Carrier et al.*, 2015]. A magma reservoir (radius $a_r$, depth $H_r$, and roof depth $H$) embedded in a homogeneous isotropic elastic half-space (density $\rho_r$ and shear modulus $G$) is fed by magma through a cylindrical conduit (radius $a_c$ and length $H_c$). Shear modulus $G$ is assumed to decrease homogeneously with the damage (see text for details) and therefore with time $t$. Pressure $P_s$ at the base of the conduit is assumed to be constant. The magma is characterized by its viscosity $\mu$ and density $\rho_m$.

no leak or addition of magma outside the magma conduit. At each time, the magma flow that rises in the conduit (given by Poiseuille's law) is equal to the time derivative of the reservoir volume variation (given by, e.g., *Delaney and McTigue* [1994]; see Figure 3 for the meaning of the symbols):

$$\frac{\pi a_c^4}{8\mu H_c}\left(P-\Delta P(t)\right)=\pi a_r^3\frac{\mathrm{d}}{\mathrm{d}t}\left(\frac{\Delta P(t)}{G(t)}\right) \tag{1}$$

that can be written as

$$\frac{\mathrm{d}\Delta P(t)}{\mathrm{d}t}=\frac{G(t)a_c^4}{8\mu H_c a_r^3}\left(P-\Delta P(t)\right)+\frac{\Delta P(t)}{G(t)}\frac{\mathrm{d}G(t)}{\mathrm{d}t}. \tag{2}$$

$P=\Delta P_s-\Delta P_r^0+\left(\rho_r-\rho_m\right)gH_c$ is a constant term, where $\Delta P_s$ is the overpressure at the source (the mantle at the base of the conduit), $\Delta P_r^0$ is the initial overpressure in the reservoir, and $\rho_r$ is the rock density. $\Delta P_r(t)=\Delta P_r^0+\Delta P(t)$ is the overpressure in the reservoir, and $\Delta P(t)$ is the change in overpressure in the reservoir since the initial time.

In the case where $G(t)$ does not explicitly depend on $\Delta P(t)$ and can be directly written as a function of the time $t$, equation (2) is a linear first-order differential equation, although with nonconstant coefficients. If $G(t)$ is known, this can be resolved using a fourth-order Runge-Kutta scheme. In *Carrier et al.* [2015], a simple damage model was used to express $G$ implicitly as a function of time. When the medium is considered to be linear elastic, $G=G_0$ is a constant, the second term on the right-hand side of equation (2) vanishes, and equation (2) becomes a simple first-order linear differential equation with constant coefficients, the solution of which is analytical:

$$\Delta P(t)=P\left(1-e^{-\frac{t}{\tau_0}}\right) \tag{3}$$

In the linear elastic case, $P$ is therefore the limit overpressure at equilibrium, and $\tau_0=\frac{8\mu H_c a_r^3}{G_0 a_c^4}$ is the characteristic time of the feeding system.

Surface displacements are computed by taking into account the free-surface effect [see, e.g., *Lisowski*, 2007]:

$$u(t)=\begin{pmatrix}u_x(t)\\u_y(t)\\u_z(t)\end{pmatrix}=\frac{\Delta P(t)}{G(t)}\chi \tag{4}$$

where $\chi=a_r^3(1-\nu)\left\{1+\left(\frac{a_r}{H_r}\right)^3\left(\frac{1+\nu}{10-14\nu}+\frac{15}{4}\left(\frac{H_r}{R}\right)^2\frac{\nu-2}{5\nu-7}\right)\right\}\begin{pmatrix}x/R^3\\y/R^3\\H_r/R^3\end{pmatrix}$, $R=\sqrt{x^2+y^2+H_r^2}=\sqrt{r^2+H_r^2}$, $r$ is the horizontal distance to the pressure source, and $\nu$ is the Poisson coefficient. A limit linear elastic displacement $u_{\mathrm{el}}$ can be defined as

$$u_{\mathrm{el}}=\frac{P}{G_0}\left|\chi\right| \tag{5}$$

where $|\chi|$ is the norm of $\chi$.

### 3.2. Understanding the Nonlinear Magma-Edifice Coupling

#### 3.2.1. A General Semianalytical Solution for the Reservoir Overpressure

Going further into the understanding of the pressure and displacement obtained by equations (2) and (4) requires analysis of these equations to provide evidence for the contribution of both the feeding system and the volcanic edifice damage. Equation (2) can be written as

$$\frac{\mathrm{d}\Delta P(t)}{\mathrm{d}t}+\left(\frac{1}{\tau_0}\frac{G(t)}{G_0}-\frac{\mathrm{d}}{\mathrm{d}t}\ln\frac{G(t)}{G_0}\right)\Delta P(t)=\frac{P}{\tau_0}\frac{G(t)}{G_0} \tag{6}$$

which is

$$\frac{\mathrm{d}\Delta P(t)}{\mathrm{d}t}+\frac{1}{\tau(t)}\Delta P(t)=\frac{P}{\tau_0}\frac{G(t)}{G_0} \tag{7}$$

where

$$\frac{1}{\tau(t)} = \frac{1}{\tau_0}\frac{G(t)}{G_0} - \frac{\mathrm{d}}{\mathrm{d}t}\ln\frac{G(t)}{G_0} \tag{8}$$

and $\tau(t)$ is the characteristic time that results from both the feeding and the damage processes.

Equation (7) is a linear ordinary differential equation, the solution of which is found from the solution of the homogeneous equation:

$$\frac{\mathrm{d}\Delta P(t)}{\mathrm{d}t} + \frac{1}{\tau(t)}\Delta P(t) = 0 \tag{9}$$

by varying the integration constant using the Euler-Lagrange method. The general solution of the inhomogeneous equation (7) is therefore

$$\Delta P(t) = P\left(\frac{\int G(t)e^{\int \frac{dt}{\tau(t)}}\mathrm{d}t}{G_0\tau_0} + K\right)e^{-\int \frac{\mathrm{d}t}{\tau(t)}} \tag{10}$$

where $K$ is a constant that is found from the initial condition $\Delta P(0) = 0$.

### 3.2.2. Modeling Damage in the Volcanic Edifice

#### 3.2.2.1. Brittle Elastic Damage Laws

*Lemaitre* [1994] defined damage as the process that leads an initially intact solid material to rupture. Damage was first defined by *Kachanov* [1958], who proposed the generalization of the concept of Young's modulus to the case where the stress-strain curve was not strictly linear and where the elastic moduli were weakened by the progressive rupture process. He proposed that the elastic moduli were linearly weakened and defined an apparent or effective Young's modulus as

$$E' = (1 - D)E \tag{11}$$

where $D$ is the damage coefficient. This is actually a brittle elastic damage approach, as Young's modulus only is decreased by the occurrence of microruptures, and no explicit plastic damage is defined. This approach has been shown by *Pijaudier-Cabot et al.* [2006] to be able to model the stress-strain curve of concrete samples even for large postpeak strain in tension tests. The damage coefficient can be defined as the ratio of the damaged or ruptured surface to the total surface for a mode I crack. *Kachanov* [1958] also defined the continuity $\Psi = 1 - D$ and the effective stress $\sigma' = \frac{\sigma}{\Psi}$ that were actually applied on the undamaged area. From numerous experimental results on material rupture, *Kachanov* [1958] proposed a law for the time evolution of the continuity $\Psi$ as

$$\Psi(t) = \left(1 - \frac{t}{t_c}\right)^a \tag{12}$$

where $t_c$ is the critical or rupture time and $a$ is a constant that characterizes the material. This law is widely used in materials sciences. It was shown by *Kachanov* [1958] that this is a solution of the differential equation:

$$\frac{\mathrm{d}\Psi}{\mathrm{d}t} = -A_K\left(\frac{\sigma_0}{\Psi}\right)^n \tag{13}$$

where the continuity $\Psi$ decreases as a power of the effective applied stress $\frac{\sigma_0}{\Psi}$; $\sigma_0$ is the tensile stress applied to the solid material, which is assumed to be constant and larger than the yield stress; and $A_K > 0$ and $n \geq 1$ are constants. By integration of equation (13) with the initial condition $\Psi(t = 0) = 1$, it is found that

$$\Psi(t) = \left(1 - A_K\,(n+1)\,{\sigma_0}^n t\right)^{\frac{1}{n+1}} \tag{14}$$

which yields $t_c = \left(A_K\,(n+1)\,{\sigma_0}^n\right)^{-1}$ and $a = \frac{1}{n+1}$. A more complete discussion of the damage laws and especially those proposed by *Fukuzuno* [1985]; *Voight* [1988]; *Krajcinovic* [1996]; *Lyakhovsky et al.* [1997]; *Turcotte et al.* [2003], is provided in Text S1 in the supporting information. *Das and Scholz* [1981] provided a similar law for the crack length increase with time during subcritical crack growth, with a very simple reasoning. All of these approaches lead to the damage law given by equations (12) and (14).

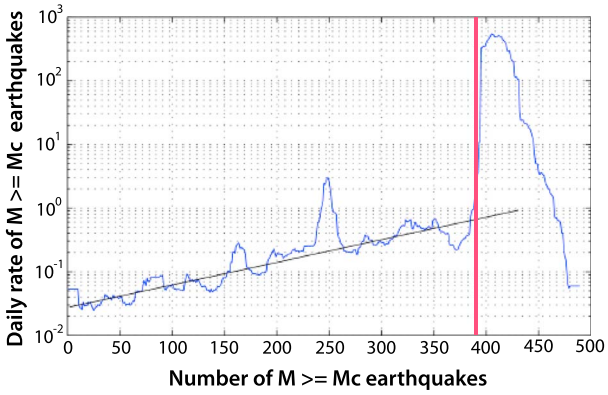


**Figure 4.** Daily rate of $M \geq M_c = 1.3$ earthquakes (smoothed on 10 earthquake windows) that occurred in the area defined by Figure 1, as a function of the cumulative number of these earthquakes. The solid line represents the linear fit that was used to compute the slope $c$ and the $\kappa$ parameter (equations (16)–(18)) up to the eruption time (vertical red line), which yielded $c \approx \frac{\ln(10)}{300}$ and $\kappa = \frac{1}{c} \approx 130$.

#### 3.2.2.2. Modeling Seismicity and Damage During the 2004–2011 Intereruptive Period at Grimsvötn Volcano

Figure 4 shows the seismicity rate $n(t)$ smoothed over 10 earthquake windows as a function of the cumulative earthquake number $N(t)$. This shows a log-linear trend, that is,

$$\ln n(t) = cN(t) + \beta \tag{15}$$

where $\beta$ and $c$ are two constants and $n(t) = \frac{dN(t)}{dt}$. Therefore, $N(t)$ is the solution of the equation:

$$\frac{dN(t)}{dt} = Be^{cN(t)} \tag{16}$$

with $B = e^{\beta}$ and $N(t = 0) = 0$; we find $N(t) = -\frac{1}{c}\ln(1 - cBt)$. We can define the critical or rupture time $t_c = \frac{1}{cB} = \frac{\kappa}{B}$, with $\kappa = \frac{1}{c}$, i.e., as a function of the seismicity parameters only. Equation (16) was already found by *Kilburn* [2003].

Therefore,

$$N(t) = -\kappa \ln\left(1 - \frac{t}{t_c}\right) \tag{17}$$

which leads to the seismicity rate

$$n(t) = \frac{\kappa}{t_c - t}. \tag{18}$$

Equation (18) shows that the seismicity rate before the 2011 eruption of Grimsvötn volcano was a simple inverse Omori law, with $\kappa \approx 130$ (Figure 4), such that $\frac{1}{n(t)}$ is a linear function, and $t_c$ can also be estimated from $\frac{1}{n(t=t_c)} = 0$ (*Voight* [1988]). The continuity $\Psi(t)$ can also be written as a function of the seismicity rate: $\Psi(t) = \left(\frac{n(t=0)}{n(t)}\right)^a$ if $\Psi(t = 0) = 1$.

*Cox and Meredith* [1993] and *Amitrano and Helmstetter* [2006] have shown how acoustic emission and microseismicity are related to damage, while *Amitrano and Helmstetter* [2006] modeled progressive damage and shear modulus decrease with time as

$$G(t) = G_0(1 - \delta)^{N(t)} \tag{19}$$

where $\delta$ is the incremental damage, i.e., the average damage per earthquake (ratio of the earthquake rupture area to the total area to be ruptured) in the time series $N(t)$. Figure S1 in the supporting information shows that the earthquake rupture area remains almost constant during the intereruptive period. Using equation (17), we can write

$$G(t) = G_0(1 - \delta)^{-\kappa \ln\left(1 - \frac{t}{t_c}\right)}, \tag{20}$$

that is,

$$G(t) = G_0 \left(1 - \frac{t}{t_c}\right)^a \tag{21}$$

where

$$a = -\kappa \ln(1 - \delta). \tag{22}$$

For $\delta << 1$,

$$a \approx \kappa\delta. \tag{23}$$

The values of $\delta$ were found to vary from $10^{-4}$ to $10^{-3}$ in *Carrier et al.* [2015]. In the present study, from $a \approx 0.33$, $\kappa \approx 130$, and equation (23), we infer $\delta \approx 2.5 \times 10^{-3}$.

As a conclusion, in equation (21) we retrieve the time variation found (equation (A7) in the supporting information) for the shear modulus from the *Kachanov* [1958] and *Voight* [1988] damage laws, although our result arises directly from seismicity data analysis and a simple incremental damage law. All three approaches are convergent to express damage as a function of time; this shows how the pre-eruptive seismicity rate can be linked to Kachanov's kinetic brittle elastic damage law. This also shows that the acceleration of pre-eruptive seismicity does not necessarily imply an increase in the reservoir overpressure.

#### 3.2.3. An Analytical Solution for Pressure and Displacement When *G* is an Explicit Function of Time

When $G(t)$ is given by equation (21), the characteristic time (equation (8)) becomes

$$\frac{1}{\tau(t)} = \frac{1}{\tau_0}\left(1 - \frac{t}{t_c}\right)^a + \frac{a}{t_c - t}. \tag{24}$$

Integration of the homogeneous equation (9) with this expression of $\frac{1}{\tau(t)}$ gives

$$\frac{\mathrm{d}\Delta P(t)}{\Delta P(t)} = -\left(\frac{1}{\tau_0}\left(1 - \frac{t}{t_c}\right)^a + \frac{a}{t_c - t}\right)\mathrm{d}t, \tag{25}$$

that is,

$$\ln\frac{\Delta P(t)}{C} = \frac{t_c}{(a+1)\tau_0}\left(1 - \frac{t}{t_c}\right)^{a+1} + a\ln\left(1 - \frac{t}{t_c}\right) \tag{26}$$

where $C$ is a constant. The general solution of the homogeneous equation (9) is

$$\Delta P(t) = C\left(1 - \frac{t}{t_c}\right)^a \mathrm{e}^{\alpha\left(1 - \frac{t}{t_c}\right)^{a+1}} \tag{27}$$

where $\alpha = \frac{t_c}{(a+1)\tau_0}$.

Using the Euler-Lagrange variation of the constant $C$, we compute the general solution of the heterogeneous equation (7) and find the overpressure in the magma reservoir (see Text S2 in the supporting information for details of the proof):

$$\frac{\Delta P(t)}{P} = \alpha^{1-s}\left(1 - \frac{t}{t_c}\right)^a \left(\gamma(s,\alpha) - \gamma\left(s, \alpha\left(1 - \frac{t}{t_c}\right)^{a+1}\right)\right)\mathrm{e}^{\alpha\left(1 - \frac{t}{t_c}\right)^{a+1}}, \tag{28}$$

and the displacement is

$$\frac{u(t)}{u_{\mathrm{el}}} = \alpha^{1-s}\left(\gamma(s,\alpha) - \gamma\left(s, \alpha\left(1 - \frac{t}{t_c}\right)^{a+1}\right)\right)\mathrm{e}^{\alpha\left(1 - \frac{t}{t_c}\right)^{a+1}} \tag{29}$$

where

$$\gamma(s,x) = \int_0^x \mathrm{e}^{-t} t^{s-1}\mathrm{d}t \tag{30}$$

is the lower incomplete gamma function and $u_{\mathrm{el}}$ is the limit displacement in the linear elastic case (equation (5)).

The linear elastic solution for $u(t)$ is retrieved from equation (29) as a special case where $a = 0$, that is, $s = 1$ and $\alpha = \frac{t_c}{\tau_0}$.

When $t$ tends to $t_c$, $\gamma\left(s, \alpha\left(1 - \frac{t}{t_c}\right)^{a+1}\right)$ tends to 0 and

$$\frac{\Delta P(t)}{P} \sim \alpha^{1-s}\gamma(s,\alpha)\left(1 - \frac{t}{t_c}\right)^{a} = \alpha^{1-s}\gamma(s,\alpha)\Psi(t), \tag{31}$$

and $\frac{u(t)}{u_{el}}$ tends to $\alpha^{1-s}\gamma(s,\alpha)$, i.e., a finite value.

Equation (28) can be rewritten as

$$\frac{\Delta P(t)}{P} = \frac{G(t)}{G_0}\frac{u(t)}{u_{el}} = \Psi(t)\frac{u(t)}{u_{el}}. \tag{32}$$

As far as the homogeneous isotropic Kachanov damage and incompressible magma hypotheses hold, the time evolution of the overpressure $\frac{\Delta P(t)}{P}$ can be inferred directly from the knowledge of the displacement data $u(t)$ and the damage law $\Psi(t) = \frac{G(t)}{G_0}$.

Magma flow can be derived directly from Poiseuille's law:

$$Q(t) = \frac{\pi a_c^4}{8\mu H_c}\left(P - \Delta P(t)\right) \tag{33}$$

from which we can write

$$Q(t=0) = Q_0 = \frac{\pi a_c^4}{8\mu H_c}P \tag{34}$$

and

$$\frac{Q(t)}{Q_0} = 1 - \frac{\Delta P(t)}{P}. \tag{35}$$

From the reservoir overpressure and magma flow, we can derive the normalized strain power:

$$\Pi(t) = \frac{\Delta P(t)Q(t)}{PQ_0} = \frac{\Delta P(t)}{P}\left(1 - \frac{\Delta P(t)}{P}\right). \tag{36}$$

## 4. Results

Figure S2 in the supporting information shows that the seismicity model given by equation (17) correctly fits the time series of the cumulative number of earthquakes. This allows estimation of $\kappa$ and $t_c$ (Figure S3 in the supporting information). Both of these parameters are progressively more resolved with time, and the values estimated in the last period were $\kappa = 130 \pm 20$ and $t_c = 2300 \pm 75$ days. The seismicity model departs from the data just before the eruption, which might be due to earthquake cascading.

Computation of the model state variables (i.e., reservoir overpressure and magma flow) requires the estimation of the model parameters $u_{el}$, $\tau_0$ and $a$ through the fitting of the horizontal displacement model $u(t)$ to the data (Figure 5). The characteristic time $\tau_0$ and the limit linear elastic displacement $u_{el}$ are mainly constrained by the first 2 year transient portion of the displacement data, whereas the damage parameter $a$ is mainly constrained by the last 5 year steady rate phase. The displacements computed with this model fit remarkably well the transient displacements that correspond to the progressive pressurization of the magma reservoir and the linearly increasing displacement recorded at GFUM. The results (Figures 5 and S4) show that the root-mean-square of the residuals can be as low as ~0.01 m. We estimated $\tau_0$ to be $\sim 250 \pm 50$ days over the first 2 years, although the use of the complete time series (which downweighs the initial portion of the signal) would lead to $\sim 300 \pm 100$ days instead (Figures 5 and S4). The limit linear elastic displacement $u_{el}$ that allows the exponential decay rate to be fit by a linear elastic model is found to be $\sim 0.20 \pm 0.02$ m. Damage parameter $a$ is found to be $\sim 0.33 \pm 0.1$. The trade-offs between these three phenomenological parameters (Figure S4 in the supporting information) are mainly controlled by the relative weight and number of measurements between the transient and steady rate portion of the displacement time series, and by outliers due to seasonal fluctuations. With the characteristic time best estimated in the transient part, and close to

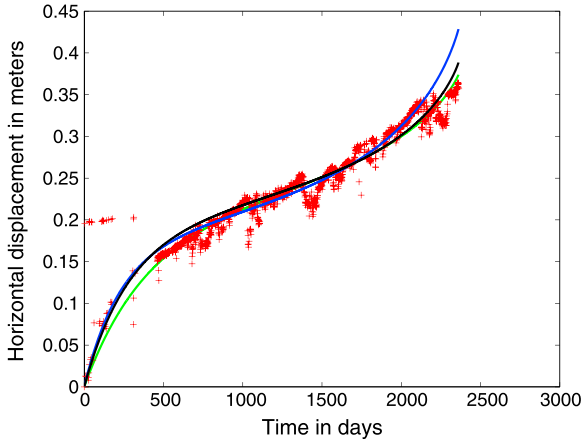


**Figure 5.** Horizontal displacement norm in meters as a function of time. Red crosses represent the data recorded at GFUM GPS station, and solid lines represent computed displacement (equation (29)) for various parameter sets: $\tau_0 = 230$ days, $a = 0.44$, $u_{el} = 0.18$ m (blue), $\tau_0 = 400$ days, $a = 0.34$, $u_{el} = 0.21$ m (green), $\tau_0 = 290$ days, $a = 0.34$, and $u_{el} = 0.20$ m (black).

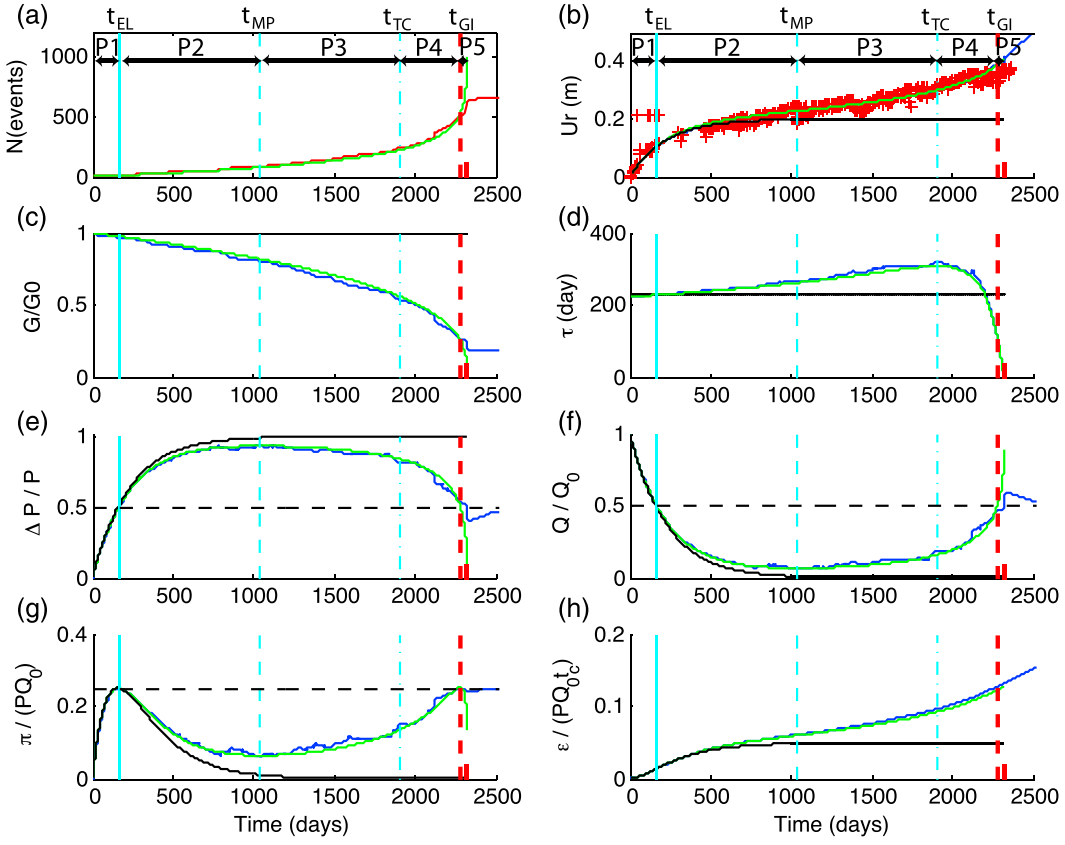


**Figure 6.** Model variables as a function of time from 1 December 2004 to 31 December 2011, computed for $\tau_0 = 250$ days, $u_{el} = 0.2$ m, and $a = 0.33$. The data are in red, the Runge-Kutta numerical solution is in blue, the analytical solution is in green, and the reference linear elastic solution is in black. (a) Cumulative number of earthquakes, (b) measured (at GFUM GPS station) and modeled horizontal displacement norm, (c) normalized shear modulus, (d) characteristic time $\tau(t)$, (e) dimensionless overpressure in the reservoir, (f) normalized magma flow rate, (g) dimensionless strain power, and (h) dimensionless strain energy. The horizontal black dashed line represents the maximum value of the strain power (0.25) and the corresponding value for the overpressure and magma flow (0.5). The vertical lines represent particular times for the following: $t_{EL}$, the linear elastic limit (solid blue); $t_{MP}$, the maximum overpressure (dashed blue); $t_{TC}$, the beginning of the tertiary creep (dash-dotted blue line); and $t_{GI}$, the generalized instability (thick dashed red). The short red tick mark represents $t_c$ and the observed eruption time. P1–P5 represent the five phases presented in section 5.

250 days in this part, we will use in the following the values $u_{el}$ = 0.2 m and $a$ = 0.33 that correspond (Figure S4 in the supporting information).

Figure 6 shows the results of the data fitting and the time history of the main variables that characterize the model. For computation of the displacement data fitting and the model variables, two complementary approaches are possible:

1. By using the cumulative earthquake number $N(t)$ directly in equation (19) and solving equation (2) using a Runge-Kutta algorithm. In this case, no seismicity model (model of $N(t)$) is needed, and no estimation of $t_c$ is performed nor needed. This was the approach chosen by *Carrier et al.* [2015];
2. By determination of a model for $N(t)$ and estimation of its parameters $\kappa$ and $t_c$ from the fit with the earthquake number time series. $t_c$ is then used in the modeling of the displacement data and the computation of the model variables. The fit of the Runge-Kutta solutions for all of the variables by the analytical solutions can also be used to estimate $t_c$. These analytical solutions allow a mean term prediction of the time variation of these variables.

Figure 6 shows that the analytical solution, which uses this seismicity model, is identical to the numerical solution, which directly uses the seismicity data, except at the very end close to the rupture and eruption.

It is a common process in Earth sciences that physical parameters that characterize a complex model are inferred from some phenomenological parameters that characterize a relatively simple signal. In the present case, the horizontal displacement signal is characterized by three phenomenological parameters; it can represent the displacement or deformation of any system that is equivalent to a damageable Kelvin model (see Text S3 in the supporting information). This signal therefore contains no information on the actual geometry of the system but rather only on the processes at work (e.g., fluid transfer, equivalent viscosity, and constitutive law of the solid). The model presented in Figure 3 is determined only using the a priori geophysical knowledge available for Grimsvötn volcano and not from the data — the data do not allow a specific element to be chosen in the class of the (phenomenological) damageable Kelvin models. Even in the framework of the model presented in Figure 3, the characteristic time $\tau_0 = \frac{8\mu H_c a_r^3}{G_0 a_c^4}$ poorly constrains the physical parameters of the model.

The results of the computation of the state variables (Figure 6) show their variations; some of them have extrema that can be used to determine particular times: (1) $t_{EL}$ coincides with the first maximum of the strain power, (2) $t_{MP}$ corresponds to the maximum reservoir overpressure, (3) $t_{TC}$ corresponds to the maximum of the characteristic time, and (4) $t_{GI}$ corresponds to the second maximum of the strain power.

These times allow periods that characterize the intereruptive process to be defined from a mechanical point of view. These features and the associated variations are presented and discussed in detail in section 5.

## 5. Discussion

### 5.1. Seismicity Analysis

The results (Figure 6) show how the accelerating seismicity recorded at Grimsvötn between 2004 and 2011 may be related to the progressive damage to the volcanic structure. A unique value of $\kappa$ allows the fitting of the earthquake time series up to $t_{GI}$ (Figure 6), i.e., during the first 2300 days. At $t_{GI}$, the seismicity accelerates, with the earthquakes clustering in space and time through triggering, which evidences a strong nonlinear process. This latter pattern strongly recalls that studied by *Kilburn* [2003] and *Collombet et al.* [2003] in the days prior to an eruption.

The damage law as a function of time (equation (21)) is characterized by the parameter $a$, which is estimated from the fit of the displacement data. Therefore, the product $a = \kappa\delta$ does not depend on the cut-off magnitude used for the counting of the earthquakes; this cut-off magnitude is often taken to be equal to the completeness magnitude $M_c$. When this cut-off magnitude is lowered, $\kappa$ becomes larger and $\delta$ becomes smaller. The physical basis of this can be found in the earthquake scaling laws. In Text S4 in the supporting information we demonstrate the relation between the damage parameter $a = \kappa\delta$ and the $b$ value:

$$a \sim 10^{(1-b)M_c}. \tag{37}$$

As $a = \kappa\delta$ is independent of the cut-off magnitude, this is compatible with the $b \sim 1$ value commonly found in tectonic areas (in the present study, $b$ is ≈0.95).

### 5.2. Displacement Modeling

The characteristic time $\tau_0$ value is 250 days at Grimsvötn volcano, whereas it was 25 days at Piton de la Fournaise [*Carrier et al.*, 2015]. This long characteristic time and the amplitude of the pressurization make the pressurization phase easily observable. It is likely that this ratio of 10 between these characteristic times is related to the ratio between the volumes of the magma reservoirs and to the difference in pressure changes. This feature might be related to the respective edifice strengths, which in part control the largest possible overpressure. This may explain this ratio of 10 more likely than a difference in the basal pressure in the mantle. Piton de la Fournaise indeed has an unstable flank, whereas Grimsvötn does not.

The damage exponent $a$ is found to be close to $\frac{1}{3}$, i.e., $n \sim 2$ in equation (13), as proposed by *Lyakhovsky et al.* [1997]: the damage rate is proportional to the strain squared. This value might be linked to the tensile state of the stress and the progressive localization of the damage along a plane.

The estimation of $u_{el}$, $\tau_0$, and $a$ that is obtained by fitting the displacement data allows computation of the model state variables (i.e., reservoir overpressure and magma flow). The uncertainty induced in the model variables by the uncertainty in the parameter estimation (Figures S5–S7 in the supporting information) does not change their general time behavior. The sources of uncertainty that are related to the spatial distribution of the damage are discussed in paragraph 5.2.2.

#### 5.2.1. Characteristic Time

The characteristic time variation as a function of time shows a remarkable pattern, with a maximum at

$$t_{TC} = \left(1 - \left(\frac{\tau_0}{t_c}\right)^s\right) t_c. \tag{38}$$

This time $t_{TC}$ separates the pre-eruptive period into two subperiods:

1. For $t \leq t_{TC}$, the order of magnitude of the characteristic time is controlled by the value of $\tau_0$ (equation (24)), i.e., by the magma transfer. During this time, the pre-eruptive process is weakly nonlinear and each variable of the model shows steady evolution (Figure 6).
2. For $t \geq t_{TC}$, the characteristic time is dominated by the second term of equation (24):

$$\frac{a}{t_c - t} = \frac{\kappa\delta}{t_c - t} = n(t)\delta; \tag{39}$$

i.e., by the rate of the new rupture area creation. It is therefore controlled by the damage process. This phase is thus equivalent to tertiary creep in the volcanic edifice. The pre-eruptive process becomes more strongly nonlinear, and the seismicity and most of the model variables show acceleration. Due to the stronger, postpeak, decrease in edifice strength (reaction), the reservoir volume increases more rapidly than the input magma flow, and the reservoir pressure decreases.

#### 5.2.2. Shear Modulus and Damage

The computations show that at GFUM, the secant shear modulus $G(t)$ decreased by about 75% in about 7 years, with this station located in the most strongly deforming volume (Figure 1). Figure 7b shows that this decrease in secant shear modulus corresponds to a drop of 50% in the rock strength, what is usual in rock mechanics experiments [see, e.g., *Jaeger et al.*, 2007]. The published elastic moduli and their variations have various values that depend mostly on the scale and the strain used for the measurement. It is well known that rock fracturing and damage decrease the Young's modulus [see, e.g., *Walsh*, 1965; *Budiansky and O'Connell*, 1976; *Kemeny and Cook*, 1986]. *Heap et al.* [2009] reported a 30% decrease in the Young's modulus during increasing amplitude cyclic stressing experiments of Etna basalt. The measured elastic moduli are equivalent moduli of the homogeneous model that represents an actually heterogeneous, fractured medium. The fracturation increases with the scale. From rock mechanics experiments, the Young's modulus for unfractured dense basalt is about 50 GPa to 75 GPa at the sample scale, whereas it can be as low as 5 GPa at the large scale [see, e.g., *Schultz*, 1993]. *Cayol and Cornet* [1998] chose a Young's modulus of 5 GPa at Piton de la Fournaise, La Réunion. This value is close to the ~3 GPa reported by *Rubin and Pollard* [1987] from estimates of dyke thicknesses at Kilauea, Hawaii. *Gudmundsson* [1988] determined a Young's modulus of ~7 GPa for the upper Icelandic crust. All of these values are 80% to 90% lower than those measured at the sample scale. In the present model, a similar spatial homogenization approach was used, as the strain or time variation of the secant shear modulus was considered to be homogeneous in the whole medium. In a fractured medium, large strain and seismicity localize along boundaries that limit unfractured blocks that experience little internal

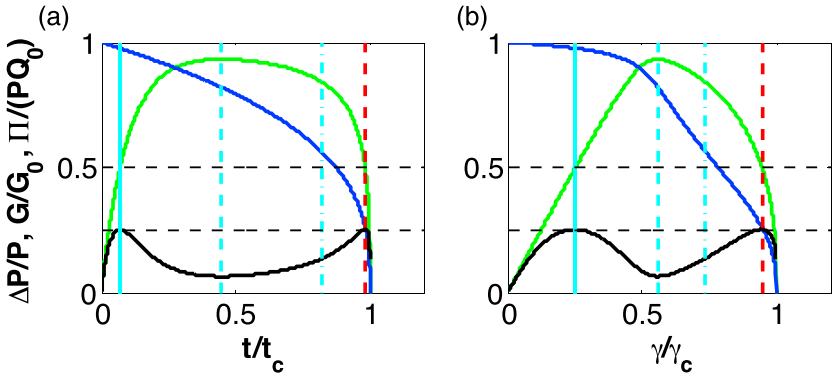


**Figure 7.** Reservoir overpressure (green), strain power (black), and shear modulus (blue) as functions of (a) normalized time $\frac{t}{t_c}$ and (b) normalized shear strain $\frac{\gamma}{\gamma_c}$; $\gamma_c$ is the shear strain at the rupture time $t_c$. Particular times are represented by the blue lines (solid: $t_{EL}$; dashed: $t_{MP}$; and dash dotted: $t_{TC}$) and the red dashed line ($t_{GI}$). Horizontal black dashed lines represent the maximum value of the strain power (0.25) and the corresponding value for the reservoir overpressure (0.5).

strain. The time variations of the apparent or equivalent shear modulus $G_{eq}$ inferred from the surface displacements in the homogeneous model are controlled by the time variations of the (low) shear modulus $G_b$ along such boundaries, where the strain and damage are large:

$$\frac{1}{G_{eq}} = \frac{1}{G_i} + \frac{1}{G_b} \tag{40}$$

where $G_i$ is the shear modulus of the intact rock [see, e.g., *Goodman*, 1989; *Jaeger et al.*, 2007]. Therefore, the time variations of the elastic moduli due to the progressive fracturation are expected to be of the same order of magnitude as the variations due to the scale effect. Moreover, the reservoir overpressure does not need to show a decreased elastic moduli over large areas to severely decrease when the magma is incompressible. In some cases, the reservoir overpressure can be controlled by the displacement of a limited area that acts like a valve. Displacement of this area has to be monitored and used as a pressure gauge, knowing the adapted damage law, which can be inferred from the seismicity.

Seismic velocity decreases have been measured before eruption using scattered elastic waves and seismic noise correlation methods [see, e.g., *Brenguier et al.*, 2008; *Clarke et al.*, 2013]. These were shown to be in the 0.1% to 1% range. They were, however, measured in large (10–100 km$^3$) and deep volumes of the volcano, whereas large internal strain and strong changes in scattering and elastic moduli are likely to be strongly localized. Averaging in smaller deformed volumes should be necessary to compare both of the estimations. However, comparison of their orders of magnitude will remain limited, as elastic waves mostly propagate in the intact rock, with a very low strain intensity.

### 5.2.3. Reservoir Overpressure and Magma Flow

The reservoir overpressure and magma flow are directly related to each other and share the same type of time variations, although of opposite signs. Seismicity appears at $t_{EL}$, when the normalized overpressure reaches 50%, which corresponds to the first maximum of the strain power. The maximum overpressure is reached at $t_{MP}$. The reservoir overpressure and magma flow remain approximately constant over a period of ~1500 days beginning before and finishing after $t_{MP}$. This is a consequence of the constant pressure condition that was imposed at the base of the magma conduit, and of the limited damage process before $t_{TC}$. Volume variation being directly proportional to surface displacement ($\Delta V(t) = \pi a_r^3 \frac{\Delta P(t)}{G(t)} = \frac{\pi a_r^3}{\chi} u(t)$), the constant inflation rate measured at the surface before and after $t_{MP}$ is the consequence of the constant volume increase rate and magma flow. After $t_{MP}$ the inflation rate is mostly controlled by the damage, with no need to impose a constant magma flow rate at the base of the conduit. The reservoir overpressure and magma flow vary more strongly after $t_{TC}$, and especially around $t_{GI}$, following the dynamics of the damage and the seismicity (equation (31)), as a consequence of the incompressible magma hypothesis. In a linear elastic edifice, the magma flow would tend to zero. When progressive damage and strain weakening occur, the magma flow increases and accelerates before the rupture. This acceleration is therefore not necessarily due to increasing magma pressure at the

base of the conduit. Such an acceleration might trigger tremors in the magma conduit, while the overpressure decrease might eventually trigger gas exsolution in the reservoir.

The surface displacement increase shows that the magma pressure decrease remains lower than the shear modulus decrease. The magma pressure in the reservoir becomes slightly larger than the edifice strength only through increased magma inflow (and not by the elastic reaction of the magma, which is incompressible). A process similar to suction limits the dynamics of the reservoir volume increase, which was already considered by *Rubin and Gillard* [1998] to explain the propagation of dykes and the surrounding seismicity. The balance between the magma flow and crack growth in magma propagation has also been studied by *Maimon et al.* [2012] with similar conclusions. At the rupture time $t_c$, the surface displacement is finite: $\frac{u(t=t_c)}{u_{el}} = \alpha^{1-s}\gamma(s,\alpha)$; this value reproduces the data relatively well. It tends to demonstrate that the magma at Grímsvötn can actually be considered as nearly incompressible, which is in agreement with what is known for basaltic magma [*Sigurdsson*, 2015].

Considering that GFUM GPS station is close to the model axis, the shear strain can be estimated by $\gamma \sim \frac{u_r}{H_r}$. With acceleration being negligible, at each time the reservoir overpressure is equal to the reaction of the edifice. The plot of reservoir overpressure as a function of $\gamma$ (Figure 7b) provides the stress-strain relationship at the scale of the volcanic edifice. The peak strength occurred at ~50% of the strain at the rupture, and accelerated yield and subsequent rupture occur far beyond the peak strength, as more than 90% strain occurred. The fit of the displacement data shows that the elasticity laws remain valid far beyond the peak strength, whereas the shear modulus decreases. The elasticity of remaining undamaged areas limits the strain when the plastic strain increases, even postpeak, as long as the plastic stress threshold is not reached at large (kilometer) scale. *Pijaudier-Cabot et al.* [2006] show that elastic damage is predominant over plastic strain during tension tests so that elastic damage models are capable of reproducing tension test stress-strain curves on concrete samples even for large postpeak strain, whereas in compression plastic damage occurs and an elastic plastic damage formulation is necessary to model compression test results. This explains why in a postpeak pressurized volcanic system experiencing orthoradial tensile stresses, the displacement recorded at one well-located GPS station can be used as a pressure gauge to estimate the time variations of the overpressure and other volcano state variables, using a pertinent elastic damage law.

#### 5.2.4. Strain Power and Energy: Investigating the Final Instability

The power computed using equation (36) is supplied by the magma to deform the magma reservoir and the surrounding edifice; we term it the strain power. This expresses the magma-edifice coupling and shows that the edifice rupture is controlled by this coupling. Its integration allows the computation of the energy $\epsilon(t)$ provided by the magma and consumed in the strain. This shows that $\epsilon(t)$ was first stored as elastic energy over ~2 years. A part (75%) of this elastic energy was then progressively released in the fracturing of the edifice when the shear modulus decreased (by 75%), whereas the continuing magma flow provided additional energy.

The form taken by equation (36) shows that the strain power necessarily reaches a maximum of $0.25PQ_0$ when $\frac{\Delta P(t)}{P} = \frac{Q(t)}{Q_0} = \frac{1}{2}$ (Figure 6). This appears to be an intrinsic property of these magma-edifice coupled systems, which expresses the magma transfer and the coupling to the edifice; this value is independent of their constitutive laws and parameter values (Figures S5–S7 in the supporting information). This maximum is first reached at time $t_{EL}$, which corresponds to the elastic limit at the end of the linear elastic pressurization phase—the beginning of the rupture process, when the seismicity rate begins to be larger than the background seismicity. This corresponds to the occurrence of the first local instabilities related to the magma reservoir pressurization. The maximum is reached a second time at the end of the rupture process, when the seismicity accelerates, clusters in time, departs from the model and is close to its maximum (Figure S2 in the supporting information). This time $t_{GI}$ corresponds to the generalized instability at the reservoir scale and the initiation of the last step of the rapid, large-scale, damage, and magma flow that precedes the rupture and the subsequent eruption. Conditions for this initiation are met when the damage is sufficient for the strain power to reach $0.25PQ_0$ or to have $\frac{\Delta P(t)}{P} = 0.5$. As time $t_{GI}$ is close to $t_c$, equation (31) can be used to express this condition:

$$\alpha^{1-s}\gamma(s,\alpha)\left(1-\frac{t_{GI}}{t_c}\right)^a = \frac{1}{2}. \tag{41}$$

We find

$$t_{GI} = \left(1 - \frac{1}{\alpha^s \left(2\gamma(s,\alpha)\right)^{\frac{1}{a}}}\right) t_c \tag{42}$$

or considering that $\alpha = s\frac{t_c}{\tau_0}$ is large so that $\gamma(s,\alpha)$ tends to $\Gamma(s)$:

$$t_{GI} = \left(1 - C\left(\frac{\tau_0}{t_c}\right)^s\right) t_c \tag{43}$$

where $C = \frac{1}{s^s(2\Gamma(s))^{\frac{1}{a}}}$. As $s = \frac{1}{a+1}$, $C$ is only controlled by $a$.

From the expressions of $t_{GI}$ and $t_{TC}$, a further estimation of $t_c$ can be inferred:

$$t_c = \frac{t_{GI} - Ct_{TC}}{1 - C}. \tag{44}$$

Using $a = \frac{1}{3}$, then $C = 0.1719$; with $t_{TC} = 1907$ days and $t_{GI} = 2279$ days then $t_c = 2356$ days, whereas the rupture and subsequent eruption actually occurred at $t_c = 2361$ days.

However, after $t_{GI}$, the earthquakes cluster in time and create discontinuities at the larger scale. The $\Delta P = 0.5P$ overpressure level that corresponds to the maximum of the strain power also corresponds to the lowest overpressure that causes seismicity at the beginning of the damage process. As the seismicity clusters for this low overpressure level, this shows that at $t_{GI}$ the edifice is very weak, close to the critical state and to the instability. The characteristic length of the seismicity cluster approaches the characteristic length to be ruptured. Therefore, rupture precedes eruption. The magma reaches the surface through a prefractured dyke with a characteristic time that is controlled by a Poiseuille law that involves the height of the dyke (depth of the magma reservoir) and its width and the overpressure in the reservoir. Field observations in Iceland have frequently shown that rupture precedes eruptions—but all ruptures do not lead to eruptions [*Buck et al.*, 2006; *Hjartardottir et al.*, 2012; *Heimisson et al.*, 2015; *Sigmundsson et al.*, 2015; *Hjartardottir et al.*, 2016]; for the Grimsvötn 2011 eruption, the magma reached the surface 90 min after the rupture (P. Einarsson, personal communication, 2016).

Time $t_{GI}$ is probably the last time when the elastic laws remain valid. After that time, the plastic laws best describe the limit equilibrium, and limit analysis should be used. Therefore, the standard deviation that affects the estimation of $t_c$ given by equation (44) is expected to be large. Time $t_c$ can be used as a mean term, first-order estimator for eruption prediction, keeping in mind that it was established using elastic damage laws that are no longer valid at the rupture time: the rupture might be further delayed or advanced by small stress perturbations. During this period, a pressure drop due to an eventual jökulhlaup from the caldera lake can help to trigger the eruption [*Vogfjörd et al.*, 2005]. Intense earthquake swarms occurred in the 1–2 h preceding the 2004 and 2011 eruptions. They allowed successful short-term warning [*Vogfjörd et al.*, 2005]. In Text S5 in the supporting information, we computed and plotted the terms $t_1 = e^{\alpha\left(1-\frac{t}{t_c}\right)^{a+1}}$ and $t_2 = \frac{\sum_{k=0}^{+\infty} \frac{\alpha^k k_x (a+1)k+1}{\Gamma(s+k+1)}}{\sum_{k=0}^{+\infty} \frac{\alpha^k}{\Gamma(s+k+1)}}$, their difference, and their ratio. We show that this ratio is extremely sensitive to the final instability that occurs after $t_{GI}$.

These results and interpretations do not mean that there is no deep magma chamber below the Grimsvötn volcano; they only mean that the displacement time series recorded from 2004 to 2011 at the GFUM GPS station cannot be interpreted unambiguously as being due to the action of a system of two superimposed magma chambers in a linear elastic crust. The two interpretations are eventually not incompatible. The present model is based on the assumption that the pressure at the base of the conduit that feeds the shallow-level magma reservoir is constant when time is positive; i.e., that the feeding system is subject to a Heaviside step in pressure difference. This constant pressure boundary condition can be relaxed by computing the impulse response of the feeding system, which is a linear first-order system. Convolution of this impulse response by variable pressure at the base of the conduit can allow modeling of the magma reservoir overpressure with

various basal input pressure conditions. Conversely, the pressure history at the base of the conduit can be inferred from the deconvolution of the recorded signals from the computed impulse response.

## 6. Conclusion

In this work, we analyzed the high-quality GPS and earthquake data recorded at Grimsvötn volcano by IMO geodetic and seismic networks during the 2004–2011 intereruptive period. The surface displacement data revealed the response of the volcanic edifice to the pressurization of the magma reservoir, which started with an exponential decay rate and was followed by a constant inflation rate. We presented a model with one pressurized magma reservoir in a damaging volcanic edifice, with the magma being incompressible and the pressure at the base of the magma conduit being constant. We modeled the damage as a function of the cumulative number of earthquakes and this number as a function of time; this allowed us to express the damage as a function of time. This expression is identical to the experimental damage law of *Kachanov* [1958]. Using this damage law in our pressurization model, we derived simple analytical expressions for the pressure and displacement as functions of time. The measured and computed displacement time series were characterized by three phenomenological parameters only: the characteristic time of the feeding system, the limiting linear elastic displacement, and the damage exponent. Inversion of the displacement and seismicity data using this simple analytical model gives a very good fit and provides reliable values for these parameters.

The parameter values inferred from fitting the horizontal displacement allow computation of the shear modulus, reservoir overpressure, magma flow, strain power, and energy as functions of time. Eight variables were defined that characterize the state of the coupled magma-edifice system and define five particular times that split the intereruptive period in five characteristic phases. For each phase a mechanical characterization of the state of the volcanic edifice is inferred. During the first phase, the pressurized volcanic edifice experienced linear elastic deformation, with the seismicity at the background level. This elastic pressurization phase was limited by the time of the first strain power maximum, where the seismicity increased. During the second phase, weak damage occurred and perturbations of the elastic solutions were limited, with the maximum pressurization achieved at the end of this phase. The third phase then occurred, during which the damage continued. The characteristic time was dominated by the magma feeding. The magma reservoir overpressure and the flow showed weak nonlinear variations, and the signs of their derivatives changed at the beginning of this phase. This phase can be considered as the secondary creep of the edifice, and it was limited by the time of the characteristic time maximum. During the fourth phase, the characteristic time and therefore the pre-eruptive dynamics were dominated by the damage, which became stronger. The seismicity accelerated and the nonlinearity increased in the reservoir overpressure and magma flow. Overpressure decreased and magma flow increased. This phase is limited by the second strain power maximum, which corresponded to generalized instability close to the rupture time. The normalized strain power maxima reached the $\frac{1}{4}$ value, whereas the normalized overpressure and magma flow reached the $\frac{1}{2}$ value. These values appear to be intrinsic characteristics of the magma-edifice coupling and can be used as thresholds. This fourth phase can be understood as tertiary creep. During the fifth phase, the seismicity clustered in time. This phase corresponded to the creation of a large-scale discontinuity and finally to the rupture. The limit equilibrium was reached, and the elasticity laws were no longer applicable. The rupture and subsequent eruption can be advanced or delayed through small stress field perturbations. It was, however, remarkable that the elasticity laws remained applicable during the relatively large postpeak strain and time interval. This appears to be a characteristic feature that occurs when brittle elastic damage in tension dominates plastic damage. In this case, elasticity laws used with an elastic damage approach are relevant to study the dynamics of the processes. Rupture and eruption and most of the eruption preparation were clearly postpeak processes. Our analysis provides reference times, phases, and variables to assess the state of the pressurized volcanic edifice, especially close to the instability. The direct Runge-Kutta numerical solutions allowed computation of the model variables without knowing the critical time. The fit of the data and the numerical solutions by the analytical values allowed the computation and mean term prediction of the time variations of these variables. The use of this analysis on other basaltic volcanoes now needs to be investigated and especially when the pressurization can be limited by the plastic displacement of a flank. This framework can be of interest in the more general case of fluid-structure interactions when the structure undergoes damage. Further work needs to be devoted to a complete stability analysis of the magma-edifice coupling close to the rupture, to the case of a compressible fluid, and to the case of variable pressure at the base of the magma conduit.

**Acknowledgments**
This work was supported by a grant from Labex OSUG@2020 (Investissements d avenir ANR10 LABX56) Université Grenoble-Alpes. The authors warmly thank Sigrun Hreinsdottir, who kindly provided Figure 1 and reviewed the manuscript; Alain Bürgisser, Jérôme Weiss, and François Nicot for reviewing and discussing the manuscript; and Pall Einarsson and an anonymous reviewer for their constructive comments. The data are available upon request to the Icelandic Meteorological Office (http://en.vedur.is/).

## References

Albino, F., V. Pinel, and F. Sigmundsson (2010), Influence of surface load variations on eruption likelihood: Application to two Icelandic subglacial volcanoes, Grímsvötn and Katla, *Geophys. J. Int.*, *181*, 1510–1524.

Alfaro, R., B. Brandsdóttir, D. P. Rowlands, R. S. White, and M. T. Gudmundsson (2007), Structure of the Grímsvötn central volcano under the Vatnajökull icecap, Iceland, *Geophys. J. Int.*, *168*(2), 863–876.

Amitrano, D., and A. Helmstetter (2006), Brittle creep, damage, and time to failure in rocks, *J. Geophys. Res.*, *111*, B11201, doi:10.1029/2005JB004252.

Bell, A., J. Greenhough, M. Heap, and I. Main (2011), Challenges for forecasting based on accelerating rates of earthquakes at volcanoes and laboratory analogues, *Geophys. J. Int.*, *185*, 718–723.

Beutler, G., M. Rothacher, S. Schaer, T. Springer, J. Kouba, and R. Neilan (1999), The international GPS services (IGS): An interdisciplinary service in support of Earth sciences, *Adv. Space Res.*, *23*, 631–653.

Bilich, A., B. Schmitz, B. Gorres, G. Zeimetz, and G. Wubbena (2012), Three-method absolute antenna calibration comparison, *IGS Workshop*, *2012*(23), 631–653.

Björnsson, H., and P. Einarsson (1990), Volcanoes beneath Vatnajökull, Iceland: Evidence from radio echo-sounding, earthquakes and jökulhlaups, *Jokull*, *40*, 147–168.

Brenguier, F., N. Shapiro, M. Campillo, V. Ferrazzini, Z. Duputel, O. Coutant, and A. Nercessian (2008), Towards forecasting volcanic eruptions using seismic noise, *Nat. Geosci.*, *2*, 126–130.

Buck, W., P. Einarsson, and B. Brandsdottir (2006), Tectonic stress and magma chamber size as controls on dike propagation: Constraints from the 1975–1984 Krafla rifting episode, *J. Geophys. Res.*, *111*, B12404, doi:10.1029/2005JB003879.

Budiansky, B., and R. O'Connell (1976), Elastic moduli of a cracked solid, *Int. J. Solids Struct.*, *12*, 81–97.

Carrier, A., J.-L. Got, A. Peltier, V. Ferrazzini, T. Staudacher, P. Kowalski, and P. Boissier (2015), A damage model for volcanic edifices: Implications for edifice strength, magma pressure, and eruptive processes, *J. Geophys. Res. Solid Earth*, *120*, 567–583, doi:10.1002/2014JB011485.

Cayol, V., and F. Cornet (1998), Three-dimensional modeling of the 1983–1984 eruption at Piton de la Fournaise Volcano, Runion Island, *J. Geophys. Res.*, *103*, 18,025–18,037.

Clarke, D., F. Brenguier, J.-L. Froger, N. Shapiro, A. Peltier, and T. Staudacher (2013), Timing of a large volcanic flank movement at Piton de la Fournaise volcano using noise-based seismic monitoring and ground deformation measurements, *Geophys. J. Int.*, *195*(2), 1132–1140.

Collombet, M., J.-R. Grasso, and V. Ferrazzini (2003), Seismicity rate before eruptions on Piton de la Fournaise volcano: Implications for eruption dynamics, *Geophys. Res. Lett.*, *30*(21), 2099, doi:10.1029/2003GL017494.

Cox, S., and P. Meredith (1993), Microcrack formation and material softening in rock measured by monitoring acoustic emissions, *Int. J. Rock Mech. Min. Sci. Geomech. Abstr.*, *30*, 11–24.

Das, S., and C. Scholz (1981), Theory of time-dependent rupture in the earth, *J. Geophys. Res.*, *86*, 6039–6051.

Delaney, P., and D. McTigue (1994), Volume of magma accumulation or withdrawal estimated from surface uplift or subsidence, with application to the 1960 collapse of Kilauea Volcano, *Bull. Volcanol.*, *56*(6–7), 417–424.

Fukuzuno, T. (1985), A method to predict the time of slope failure caused by rainfall using the inverse number of velocity of surface displacement, *J. Jpn. Landslide Soc.*, *22*, 8–14.

Goodman, R. (1989), *Introduction to Rock Mechanics*, Wiley-Blackwell, New York.

Gudmundsson, A. (1988), Effect of tensile stress concentration around magma chamber on intrusion and extrusion frequencies, *J. Volcanol. Geotherm. Res.*, *35*, 179–194.

Gudmundsson, M. T., and J. Milsom (1997), Gravity and magnetic studies of the subglacial Grímsvötn volcano, Iceland: Implications for crustal and thermal structure, *J. Geophys. Res.*, *102*, 7691–7704.

Heap, M., S. Vinciguerra, and P. Meredith (2009), The evolution of elastic moduli with increasing crack damage during cyclic stressing of a basalt from Mt. Etna volcano, *Tectonophysics*, *471*, 153–160.

Heap, M., D. Faulkner, P. Meredith, and S. Vinciguerra (2010), Elastic moduli evolution and accompanying stress changes with increasing crack damage: Implications for stress changes around fault zones and volcanoes during deformation, *Geophys. J. Int.*, *183*, 225–236.

Heimisson, E., P. Einarsson, F. Sigmundsson, and B. Brandsdottir (2015), Kilometer-scale Kaiser effect identified in Krafla volcano, Iceland, *Geophys. Res. Lett.*, *42*, 7958–7865, doi:10.1002/2015GL065680.

Hjartardottir, A., P. Einarsson, E. Bramham, and T. Wright (2012), The Krafla fissure swarm, Iceland, and its formation by rifting events, *Bull. Volcanol.*, *74*, 2139–2153.

Hjartardottir, A., P. Einarsson, M. Gudmundsson, and T. Högnadottir (2016), Fracture movements and graben subsidence during the 2014 Bardarbunga dike intrusion in Iceland, *J. Volcanol. Geotherm. Res.*, *310*, 242–252, doi:10.1016/j.jvolgeores.2015.12.002.

Hreinsdottir, S., et al. (2014), Volcanic plume height correlated with magma-pressure change at Grímsvötn Volcano, Iceland, *Nat. Geosci.*, *7*, 214–218.

Jaeger, J., N. Cook, and R. Zimmermann (2007), *Fundamentals of Rock Mechanics*, Wiley-Blackwell, New York.

Kachanov, L. M. (1958), Time of the rupture process under creep conditions, *Isv. Akad. Nauk. SSR. Otd Tekh. Nauk*, *8*, 26–31.

Kemeny, J., and N. Cook (1986), Effective moduli, non-linear deformation and strength of a cracked elastic solid, *Int. J. Rock Mech. Min. Sci. Geomech. Abstr.*, *23*, 107–118.

Kilburn, C. (2003), Multiscale fracturing as a key to forecasting volcanic eruptions, *J. Volcanol. Geotherm. Res.*, *125*, 271–289.

Krajcinovic, D. (1996), *Damage Mechanics*, Elsevier, Amsterdam.

Lemaitre, J. (1994), *Mechanics of Solid Materials*, Cambridge Univ. Press, Cambridge, U. K.

Lengliné, O., D. Marsan, J. Got, V. Pinel, V. Ferrazzini, and P. Okubo (2008), Seismicity and deformation induced by magma accumulation at three basaltic volcanoes, *J. Geophys. Res.*, *113*, B12305, doi:10.1029/2008JB005937.

Lisowski, M. (2007), Analytical volcano deformation source models, in *Volcano Deformation*, edited by D. Dzurisin, pp. 279–304, Springer, Berlin.

Lu, Z., T. Masterlark, D. Dzurisin, R. Rykhus, and C. Wicks (2003), Magma supply dynamics at Westdahl volcano, Alaska, modeled from satellite radar interferometry, *J. Geophys. Res.*, *108*(B7), 2354, doi:10.1029/2002JB002311.

Lyakhovsky, V., Y. Ben-Zion, and A. Agnon (1997), Distributed damage, faulting, and friction, *J. Geophys. Res.*, *102*, 27,635–27,649.

Maimon, O., V. Lyakhovsky, O. Melnik, and O. Navon (2012), The propagation of a dyke driven by gas-saturated magma, *Geophys. J. Int.*, *189*, 956–966.

Main, I. (2000), A damage mechanics model for power-law creep and earthquake aftershock and foreshock sequences, *Geophys. J. Int.*, *142*, 151–161.

Pijaudier-Cabot, G., F. Dufour, M. Choinska, A. Krayani, L. Jason, and G. Chatzigeorgiou (2006), Some constitutive and computational aspects of coupled hydraulic-damage problems for leakage rate predictions of concrete vessels, in *Computational Modelling of Concrete Structures*, edited by G. Meschke et al., pp. 15–32, Taylor and Francis, London.

Reverso, T., J. Vandemeulebrouck, F. Jouanne, V. Pinel, T. Villemin, E. Sturkell, and P. Bascou (2014), A two-magma chamber model as a source of deformation at Grímsvötn Volcano, Iceland, *J. Geophys. Res. Solid Earth*, *119*, 4666–4683, doi:10.1002/2013JB010569.

Roberts, N., A. Bell, and I. Main (2015), Are volcanic seismic *b*-values high, and if so when?, *J. Volcanol. Geotherm. Res.*, *308*, 127–141, doi:10.1016/j.jvolgeores.2015.10.021.

Rubin, A., and D. Gillard (1998), Dike-induced earthquakes: Theoretical considerations, *J. Geophys. Res.*, *103*, 10,017–10,030.

Rubin, A., and D. Pollard (1987), Origins of blade-like dikes in volcanic rift zones, *U.S. Geol. Surv. Prof. Pap.*, *1350*, 1449–1470.

Schmid, A., J.-R. Grasso, D. Clarke, V. Ferrazzini, P. Bachèlery, and T. Staudacher (2012), Eruption forerunners from multiparameter monitoring and application for eruptions time predictability (Piton de la Fournaise), *J. Geophys. Res.*, *117*, B11203, doi:10.1029/2012JB009167.

Schultz, R. A. (1993), Brittle strength of basaltic rock masses with applications to Venus, *J. Geophys. Res.*, *98*(E6), 10,883–10,895.

Sigmundsson, F., et al. (2015), Segmented lateral dyke growth in a rifting event at Bardarbunga volcanic system, Iceland, *Nature*, *517*, 191–195.

Sigurdsson, H. (2015), *Encyclopedia of Volcanoes*, Academic Press, San Diego, Calif.

Sturkell, E., P. Einarsson, F. Sigmundsson, S. Hreinsdottir, and H. Geirsson (2003), Deformation of Grímsvötn volcano, Iceland: 1998 eruption and subsequent inflation, *Geophys. Res. Lett.*, *30*(4), 1182, doi:10.1029/2002GL016460.

Sturkell, E., P. Einarsson, F. Sigmundsson, H. Geirsson, H. Olafsson, R. Pedersen, E. de Zeeuw-van Dalfsen, A. T. Linde, S. I. Sacks, and R. Stefánsson (2006), Volcano geodesy and magma dynamics in Iceland, *J. Volcanol. Geotherm. Res.*, *150*(1), 14–34.

Tarraga, M., R. Carniel, R. Ortiz, and A. Garcia (2008), The failure forecast method: Review and application for the real-time detection of precursory patterns at reawakening volcanoes, *Dev. Volcanol.*, *10*, 447–469, doi:10.1016/S1871-644X(07)00013-7.

Tryggvason, E. (1973), Surface deformation and crustal structure in the Myrdalsjökull area of South Iceland, *J. Geophys. Res.*, *78*, 2488–2497.

Turcotte, D., and M. Glasscoe (2004), A damage model for the continuum rheology of the upper continental crust, *Tectonophysics*, *383*, 71–80.

Turcotte, D., W. Newman, and R. Shcherbakov (2003), Micro and macroscopic models of rock fracture, *Geophys. J. Int.*, *152*, 718–728.

Vogfjörd, K., et al. (2005), Forecasting and monitoring a subglacial eruption in Iceland, *Eos Trans. AGU*, *86*(26), 245–252.

Voight, B. (1988), A method for prediction of volcanic eruptions, *Nature*, *332*, 125–130.

Walsh, J. (1965), The effect of cracks on the uniaxial elastic compression of rock, *J. Geophys. Res.*, *70*, 399–411.

Wells, D., and K. Coppersmith (1994), New empirical relationships among magnitude, rupture length, rupture width, rupture area, and surface displacement, *Bull. Seismol. Soc. Am.*, *84*(4), 974–1002.

# Supporting Information for "An analysis of the non-linear magma-edifice coupling at Grimsvötn volcano (Iceland)"

Jean-Luc Got,[1,2] Aurore Carrier,[1,2] David Marsan,[1,2] François Jouanne,[1,2]

Kristin Vogfjörd,[3] Thierry Villemin[4]

**Contents of this file** Text and equations, Figures S1 to S9

**Introduction**

---

Corresponding author: J.-L. Got, ISTerre, Université de Savoie, 73376 Le Bourget-du-Lac FRANCE. (jlgot@univ-savoie.fr)

[1]Université Savoie Mont-Blanc, ISTerre,

F-73376 Le Bourget-du-Lac, France

[2]CNRS, ISTerre, F-73376 Le

Bourget-du-Lac, France

[3]IMO, Vedurstofa Islands, Bustadavegi

7-9, 108 Reykjavik, Iceland

[4]Université Savoie Mont-Blanc,

EDYTEM, F-73376 Le Bourget-du-Lac,

France

This supporting information provides:

- the text and equations for appendices:

A. Comparing damage laws

B. Computation of the constant in equation ()

C. Damageable Kelvin Model

D. Parameter a and earthquake scaling laws

E. Separating feeding and damage contributions in pressure and displacement

- the figures S1 to S9.

## 1. Comparing damage laws

*Lyakhovsky et al.* [1997] studied the kinetics of the damage process from a continuum thermodynamics point of view and reached an equation similar to equation (13), in which $n = 2$ in the case of uniaxial tensile stress (see also *Turcotte and Glasscoe* [2004])

$$\frac{d\Psi}{dt} = -A\left(\frac{\sigma_0}{E_0\Psi}\right)^2 \tag{1}$$

so that damage rate increases with the squared elastic strain. This may be understood as a scaling law, with damage propagating along a plane normal to the direction along which the uniaxial strain is measured. In this case, $a = \frac{1}{n+1} = \frac{1}{3}$ and [*Turcotte and Glasscoe*, 2004]

$$t_c = \frac{1}{3A}\left(\frac{E_0}{\sigma_0}\right)^2 \tag{2}$$

This conclusion is also reached by using fiber bundle models [*Krajcinovic*, 1996; *Turcotte et al.*, 2003].

A similar law was used in earth sciences by *Fukuzuno* [1985] who studied the rupture of soils submitted to an artificial spray on an inclined support

$$\frac{d^2x}{dt^2} = A' \left(\frac{dx}{dt}\right)^{\beta} \tag{3}$$

where $x$ is the surface displacement of the soil, $t$ is the time, $A'$ and $\beta$ are two constants inferred from experiments. *Voight* [1988] generalized this law to any observable $\Omega$ related to the physical change of the material in the vicinity of the rupture:

$$\frac{d^2\Omega}{dt^2} = A' \left(\frac{d\Omega}{dt}\right)^{\beta} \tag{4}$$

This equation is the basis of the Failure Forecast Method (FFM), used in volcanology to predict eruptions [*Voight*, 1988; *Tarraga et al.*, 2008; *Bell et al.*, 2011a, b; *Boué et al.*, 2015].

Writing $\Psi = \frac{1}{\Omega} = \frac{dt}{dx}$, we find

$$\frac{d\Psi}{dt} = -\frac{\ddot{\Omega}}{\dot{\Omega}^2} \tag{5}$$

so that using $\Omega$ as a variable, equation (13) becomes,

$$\ddot{\Omega} = A_K {\sigma_0}^n \dot{\Omega}^{(n+2)} \tag{6}$$

which can be identified with equation (4), with $A' = A_K {\sigma_0}^n$ and $\beta = n + 2$.

Therefore the equation of *Voight* [1988] (equation (4)) is similar to that of *Kachanov* [1958] (equation (13)). However *Voight* [1988] considered the inverse of the velocity $\Psi = \frac{1}{\Omega}$ as a measure of Kachanov's continuity $\Psi = 1 - D$, which is true only in the vicinity of the rupture, because $\Psi$ and $D$ are in the interval [0;1], whereas the velocity inverse tends to infinity when velocity tends to zero. Another important difference between equations (4) and (13) comes from *Voight* [1988]'s $A'$ constant, which is actually a function of the applied constraint $\sigma$, and thus not only depends on the material. However in both cases,

the continuity function $\Psi = 1 - D = \frac{1}{\dot{\Omega}}$ may be written as a function of time using equation (12). As a consequence, the effective shear modulus may be described as a function of time:

$$G(t) = (1 - D)G_0 = G_0\Psi(t) = G_0\left(1 - \frac{t}{t_c}\right)^a \tag{7}$$

$G(t)$ is a secant elastic modulus used in a finite stress - finite strain relation, which is linear at each time; it is not the tangent modulus used in incremental stress-strain relations.

## 2. Computation of the constant in equation (27)

Using Euler-Lagrange variation of the constant $C$, we compute the general solution of the heterogeneous equation (7):

$$\frac{d\Delta P(t)}{dt} + \frac{1}{\tau(t)}\Delta P(t) = \frac{dC(t)}{dt}\left(1 - \frac{t}{t_c}\right)^a \mathrm{e}^{\alpha\left(1-\frac{t}{t_c}\right)^{a+1}} = \frac{P}{\tau_0}\left(1 - \frac{t}{t_c}\right)^a \tag{8}$$

giving

$$C(t) = \frac{P}{\tau_0}\int \mathrm{e}^{-\alpha\left(1-\frac{t}{t_c}\right)^{a+1}} dt \tag{9}$$

Using the new variable

$$u = \alpha\left(1 - \frac{t}{t_c}\right)^{a+1} \tag{10}$$

we find, with $s = \frac{1}{a+1}$,

$$C(t) = -P\alpha^{1-s}\int_{\alpha}^{\alpha\left(1-\frac{t}{t_c}\right)^{a+1}} \mathrm{e}^{-u}u^{s-1}du \tag{11}$$

that is,

$$C(t) = P\alpha^{1-s}\left(\gamma(s,\alpha) - \gamma\left(s, \alpha\left(1 - \frac{t}{t_c}\right)^{a+1}\right)\right) \tag{12}$$

where

$$\gamma(s,x) = \int_0^x \mathrm{e}^{-t}t^{s-1}dt \tag{13}$$

is the lower incomplete gamma function.

## 3. Damageable Kelvin Model

In this section we show that the displacement signal represented in Figure 2 may be modeled by a damageable Kelvin model. This model may be represented as a system of one spring and one dashpot connected in parallel (Figure S8), with the spring being damaged such that its rigidity decreases with time following equation (7). This model represents, for example, a poro-elastic rock saturated by a fluid, with the pores connected and the rock matrix subject to damage.

Writing this, at equilibrium, the applied stress $\sigma_0$ is equal to the sum of the elastic reaction $\sigma_e = k\epsilon$ (where $k$ is the rigidity of the spring and $\epsilon$ is the strain) and the viscous reaction $\sigma_v = \eta\frac{d\epsilon}{dt}$ (where $\eta$ is the viscosity of the dashpot), we find that (with the elastic strain being taken as equal to the viscous strain)

$$k\epsilon + \eta\frac{d\epsilon}{dt} = \sigma_0 \tag{14}$$

with $k = k(t) = k_0\left(1 - \frac{t}{t_c}\right)^a$, where $k_0$ is the rigidity of the undamaged spring.

Solving the homogeneous equation gives $\epsilon(t) = C\mathrm{e}^{\alpha'\left(1-\frac{t}{t_c}\right)^{a+1}}$ where $\alpha' = \frac{t_c}{(a+1)\tau_0'}$, and $\tau_0' = \frac{\eta}{k_0}$ is the characteristic time of the linear elastic Kelvin model. Using Euler-Lagrange variation of the constant $C$ and the change of variable (equation (10)), we can compute the solution of the heterogeneous equation (14) as in equations (9-12)

$$\frac{\epsilon(t)}{\epsilon_{el}} = \alpha^{1-s}\left(\gamma(s,\alpha) - \gamma\left(s, \alpha\left(1 - \frac{t}{t_c}\right)^{a+1}\right)\right)\mathrm{e}^{\alpha\left(1-\frac{t}{t_c}\right)^{a+1}} \tag{15}$$

where $\epsilon_{el} = \frac{\sigma_0}{k_0}$ is the limit linear elastic strain. Equation (15) is similar to equation (29).

## 4. Parameter $a$ and earthquake scaling laws

The Gutenberg - Richter law shows that, for sufficiently long times $t$, $N(t) \sim 10^{-bM}$ where $M$ is the earthquake magnitude and $b$ is the "b-value" parameter commonly close

to 1 in seismically active regions; therefore $\kappa \sim 10^{-bM_c}$. The earthquake stress drop $\Delta\sigma$ is proportional to the shear strain $\frac{u}{L}$, where $u$ is the average slip during the earthquake and $L$ the rupture length. The independence of the stress drop from the magnitude implies that $u$ scales with $L$. Thus the seismic moment $M_0 \sim uL^2$ scales with $L^3$. The *Gutenberg* [1956] seismic moment - magnitude relation states that $M_0 \sim 10^{1.5M}$; therefore the rupture length $L$ is $\sim 10^{0.5M}$ and the rupture surface $S$ is $\sim 10^M$. The incremental damage parameter $\delta$ (which is the ratio of the damaged or ruptured area $S$ to the total surface to be ruptured during the pre-eruptive process), is therefore proportional to $S$ and scales with $M_c$ as $10^{M_c}$. This provides a relationship between the damage parameter $a = \kappa\delta$ and the b-value:

$$a \sim 10^{(1-b)M_c} \tag{16}$$

## 5. Separating the feeding and damage contributions in pressure and displacement expressions

Although equation (28) is the closed-form solution for the reservoir overpressure, it may be of interest to search for a formulation that allows us to separate, as far as possible, the contribution of the feeding system from the contribution of the edifice damage. To this aim, we used the power series expansion of the lower incomplete gamma function

$$\gamma(s,x) = x^s\Gamma(s)\mathrm{e}^{-x}\sum_{k=0}^{+\infty}\frac{x^k}{\Gamma(s+k+1)} \tag{17}$$

to express

$$\gamma(s,\alpha) = \alpha^s\Gamma(s)\mathrm{e}^{-\alpha}\sum_{k=0}^{+\infty}\frac{\alpha^k}{\Gamma(s+k+1)} \tag{18}$$

and

$$\gamma(s,\alpha x^{a+1}) = \alpha^s x\Gamma(s)\mathrm{e}^{-\alpha x^{a+1}}\sum_{k=0}^{+\infty}\frac{\alpha^k x^{(a+1)k}}{\Gamma(s+k+1)} \tag{19}$$

where $\Gamma$ is the gamma function, $x = 1 - \frac{t}{t_c}$ and $(a+1)s = 1$.

Therefore equation (28) may be rewritten as

$$\frac{\Delta P(x)}{P} = \alpha\Gamma(s)x^a \left( \mathrm{e}^{\alpha\left(x^{a+1}-1\right)} \sum_{k=0}^{+\infty} \frac{\alpha^k}{\Gamma(s+k+1)} - \sum_{k=0}^{+\infty} \frac{\alpha^k x^{(a+1)k+1}}{\Gamma(s+k+1)} \right) \tag{20}$$

or

$$\frac{\Delta P(x)}{P} = \alpha\Gamma(s)x^a \sum_{k=0}^{+\infty} \frac{\alpha^k}{\Gamma(s+k+1)} \left( \mathrm{e}^{\alpha\left(x^{a+1}-1\right)} - \frac{\sum_{k=0}^{+\infty} \frac{\alpha^k x^{(a+1)k+1}}{\Gamma(s+k+1)}}{\sum_{k=0}^{+\infty} \frac{\alpha^k}{\Gamma(s+k+1)}} \right) \tag{21}$$

Similarly the displacement may be written as

$$\frac{u(x)}{u_{el}} = \alpha\Gamma(s) \left( \mathrm{e}^{\alpha\left(x^{a+1}-1\right)} \sum_{k=0}^{+\infty} \frac{\alpha^k}{\Gamma(s+k+1)} - \sum_{k=0}^{+\infty} \frac{\alpha^k x^{(a+1)k+1}}{\Gamma(s+k+1)} \right) \tag{22}$$

or

$$\frac{u(x)}{u_{el}} = \alpha\Gamma(s) \sum_{k=0}^{+\infty} \frac{\alpha^k}{\Gamma(s+k+1)} \left( \mathrm{e}^{\alpha\left(x^{a+1}-1\right)} - \frac{\sum_{k=0}^{+\infty} \frac{\alpha^k x^{(a+1)k+1}}{\Gamma(s+k+1)}}{\sum_{k=0}^{+\infty} \frac{\alpha^k}{\Gamma(s+k+1)}} \right) \tag{23}$$

The first additive term in equations (20-23) represents the contribution of the feeding system to increase the overpressure, and the second additive term represents the contribution of the edifice damage to limit the overpressure. These terms are represented in Figure S9 . The linear elastic case corresponds to $a = 0$ that is $s = 1$; equation (3) is retrieved from equations (20, 21) after some algebra, given that $\Gamma(s+k+1) = (k+1)!$ for $s = 1$, so that $\sum_{k=0}^{+\infty} \frac{\alpha^{(k+1)}}{\Gamma(s+k+1)} = \mathrm{e}^{\alpha} - 1$ and $\sum_{k=0}^{+\infty} \frac{(\alpha x)^{(k+1)}}{\Gamma(s+k+1)} = \mathrm{e}^{\alpha x} - 1$.

Equations (20-23) allow us to define a further variable that is potentially useful to characterize the final instability. In Figure S9, we plotted the terms $t_1 = \mathrm{e}^{\alpha\left(1-\frac{t}{t_c}\right)^{a+1}}$ and $t_2 = \frac{\sum_{k=0}^{+\infty} \frac{\alpha^k x^{(a+1)k+1}}{\Gamma(s+k+1)}}{\sum_{k=0}^{+\infty} \frac{\alpha^k}{\Gamma(s+k+1)}}$, their differences and their ratios. The first term $t_1$ may be understood as due to the feeding, and the second term as due to the edifice reaction. Figure S9c shows that their difference is in the $10^{-4}$ magnitude range, though each term varies between 0 and 1. Although very small, this difference contains all the time information carried in

the surface displacement (Figure S9b). The ratio of the first to the second term shows that it remains close to one most of the time, and accelerates rapidly at the end of the process (Figure S9c). It is therefore extremely sensitive to the final dynamics of the process. Large instabilities may be generated by very small differences between action and reaction, especially when the action tends to weakens the reaction.

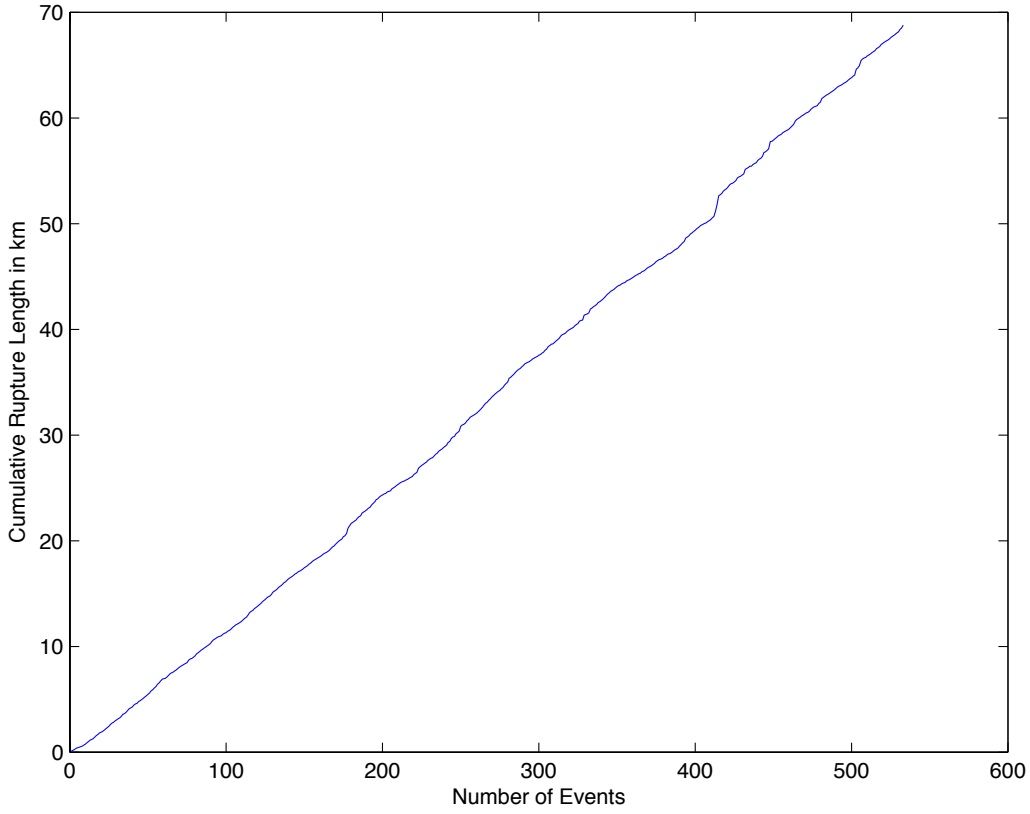


**Figure S1. Cumulative rupture length in km as a function of the number of earthquakes between 1 December 2004 to 21 May 2011 at Grimsvötn volcano. Each rupture length was computed as the square root of the rupture area $A$ deduced from the *Wells and Coppersmith* [1994] scaling law: $A = 10^{-2.87+0.82M}$, where $M$ is the local magnitude. Rupture length is almost constant with time and equal to $\sim 130$m during this period.**

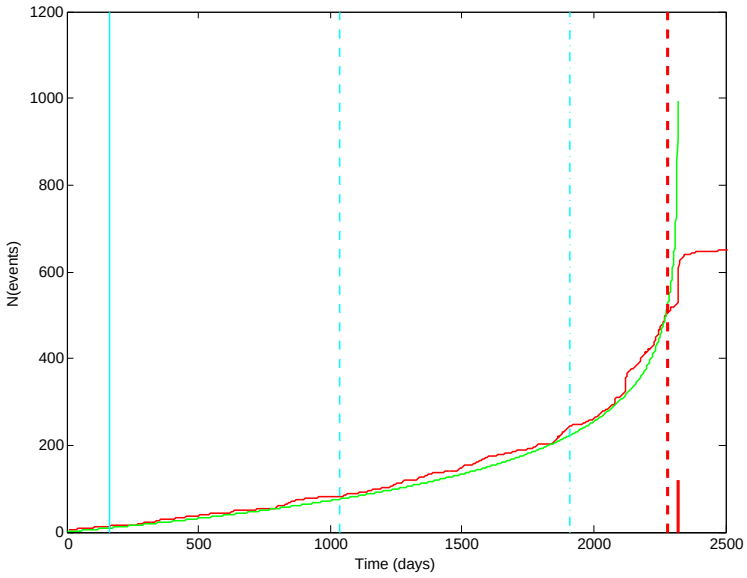


**Figure S2. Cumulative number of earthquakes as a function of time. Detailed representation showing the end of the time series. Data are represented in red, analytical solution is represented in green. See Figure 6 for the description of the particular times (vertical blue and red lines).**

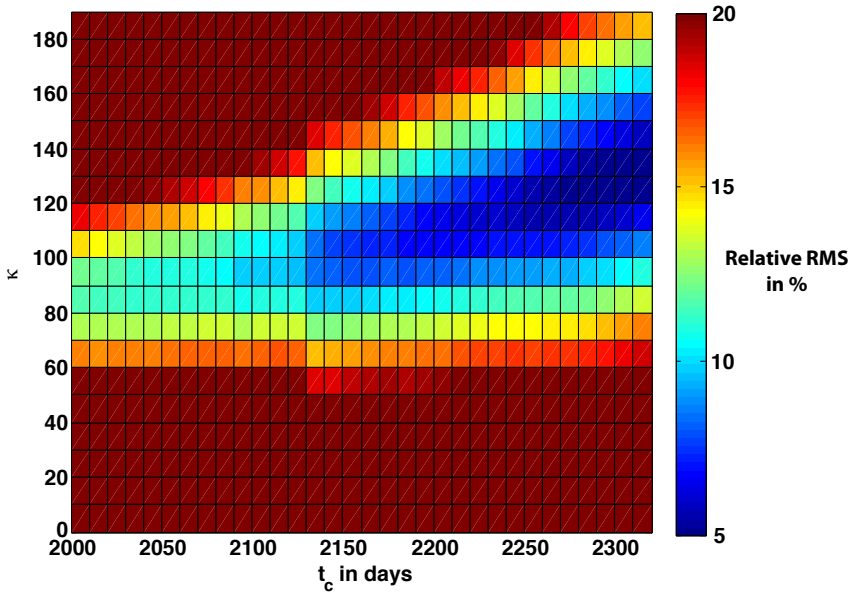


**Figure S3. Result of the exhaustive computation of the residual standard deviation (RMS) between the cumulative number of earthquakes as a function of time and its model (equation 17), as a function of $\kappa$ and $t_c$. RMS is normalized by the cumulative number of earthquakes at the corresponding $t_c$.**

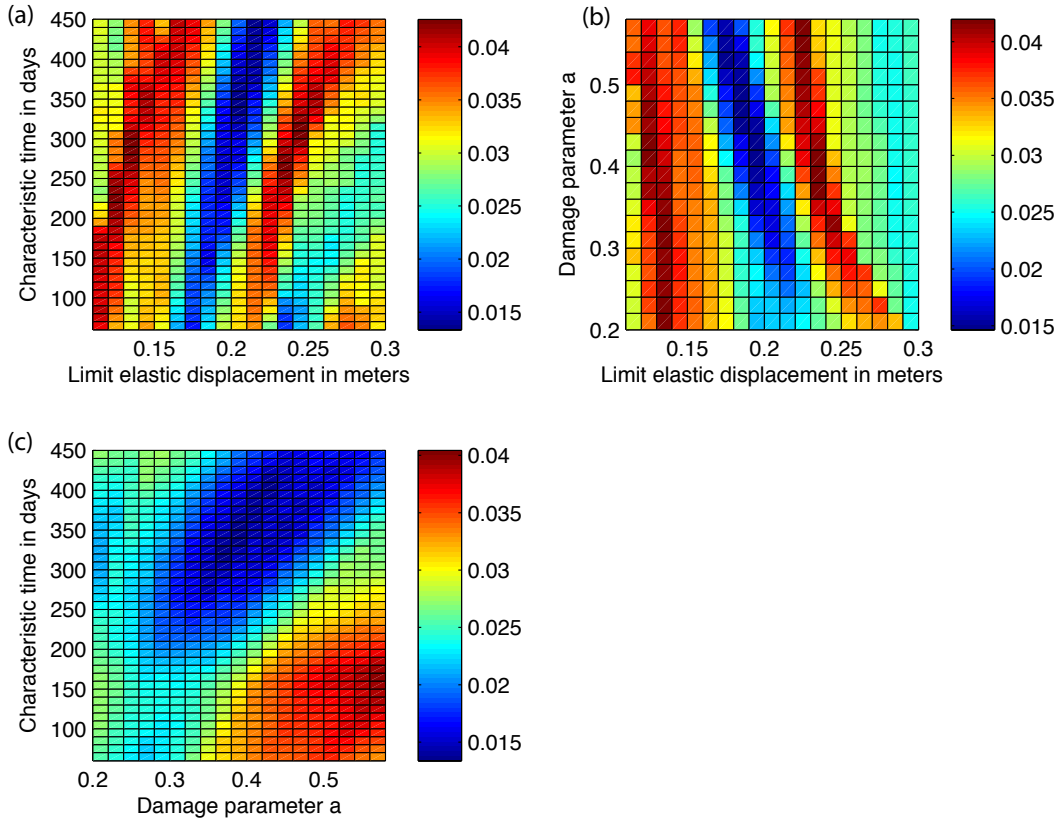


**Figure S4. Results of the exhaustive computation of the residual standard deviation (RMS) in meters, between horizontal displacement recorded at GFUM and the radial displacement computed using equation (29), for various pairs of model parameters: (a) limit elastic displacement $u_{el}$ and characteristic time $\tau_0$, (b) damage parameter $a$ and limit elastic displacement, (c) characteristic time and damage parameter.**

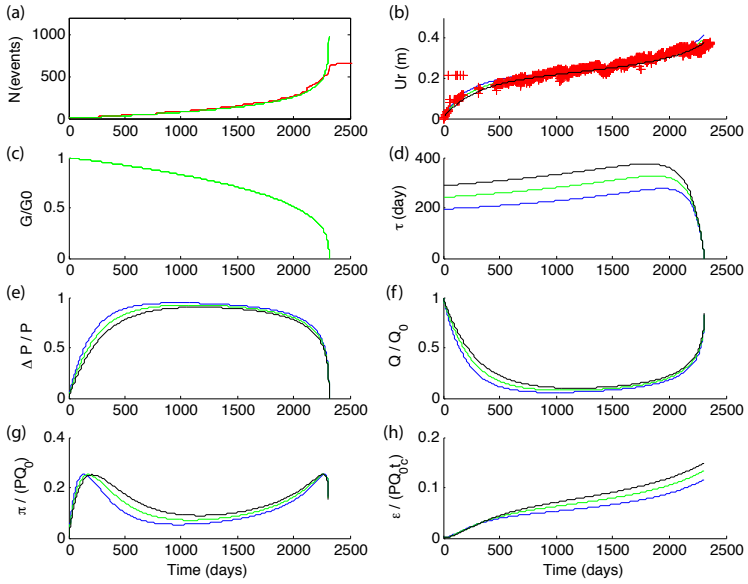


**Figure S5. Model variables as a function of time from 1 December 2004 to 31 December 2011. Red, blue, green and black colours represent respectively data, and results for various values of $\tau_0$: 200, 250 and 300 days, whereas $a = 1/3$ and $t_c$ is set to the eruption day. See Figure 9 for the description of each variable.**

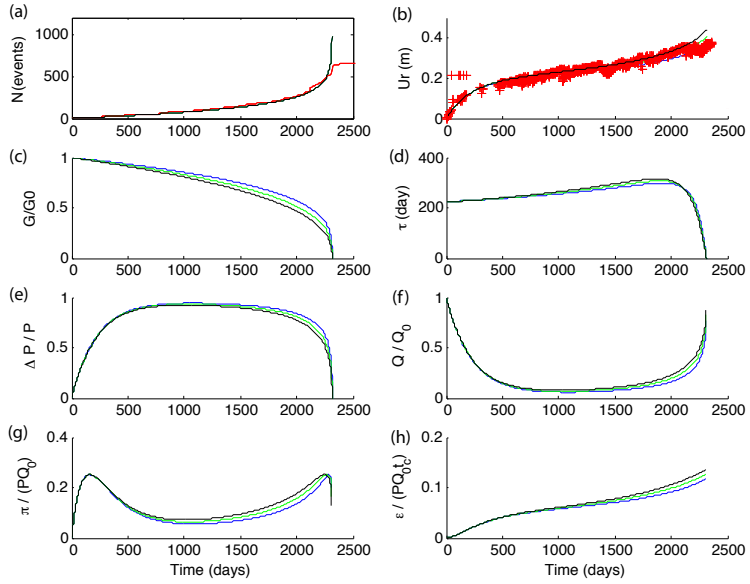


**Figure S6. Model variables as a function of time from 1 December 2004 to 31 December 2011. Red, blue, green and black colours represent respectively data, and results for various values of $a$: 0.28, 0.33 and 0.38; $\tau_0 = 250$ days and $t_c$ is set to the eruption day. See Figure 9 for the description of each variable.**

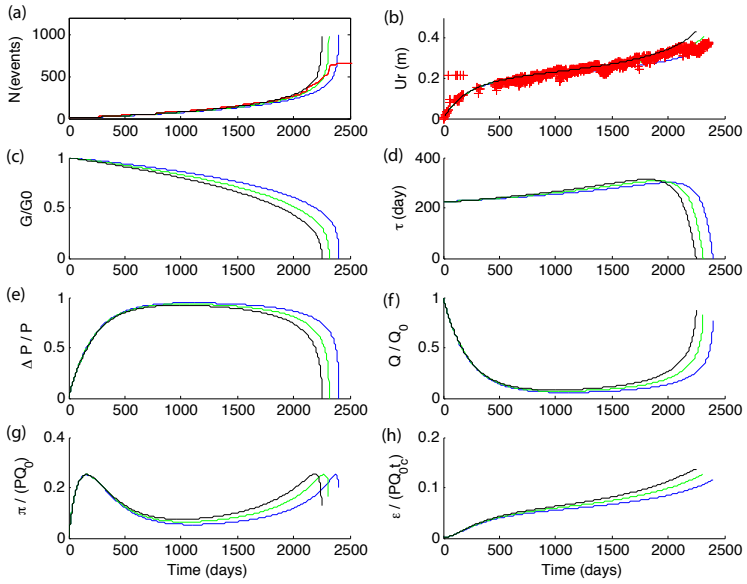


**Figure S7. Model variables as a function of time from 1 December 2004 to 31 December 2011. Red, blue, green and black colours represent respectively data, and results for various values of $a$: 0.28, 0.33 and 0.38 and corresponding $t_c$ (respectively eruption day + 100 days, eruption day and eruption day - 100 days); $\tau_0 = 250$ days. See Figure 9 for the description of each variable.**

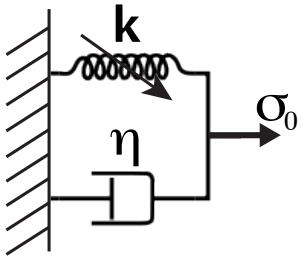


**Figure S8. Damageable Kelvin model, made up by a spring of variable rigidity $k$ in parallel with a dashpot of viscosity $\eta$. A constant stress $\sigma_0$ is applied to this system; elastic and viscous strain are considered equal.**

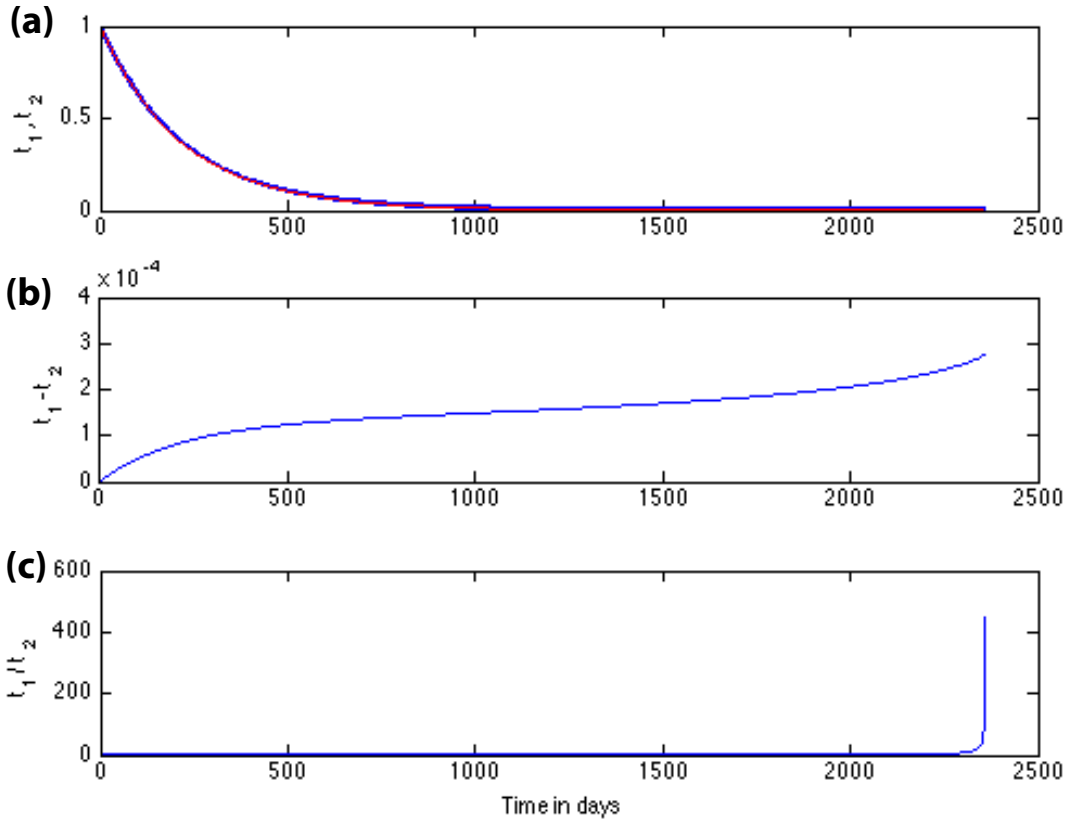


**Figure S9.** (a) Dimensionless terms $t_1 = \mathrm{e}^{\alpha\left(1-\frac{t}{t_c}\right)^{a+1}}$ (blue) and $t_2 = \frac{\sum_{k=0}^{+\infty} \frac{\alpha^k x^{(a+1)k+1}}{\Gamma(s+k+1)}}{\sum_{k=0}^{+\infty} \frac{\alpha^k}{\Gamma(s+k+1)}}$ (red), (b) their difference $t_1 - t_2$ and (c) their ratio $\frac{t_1}{t_2}$ as a function of time in days from 1 December 2004 to 31 December 2011.